Chapter 2
Theory and Applications Based on S-Gear Geometry

Gorazd Hlebanja, Miha Erjavec, Matija Hriberšek, Luka Knez, and Simon Kulovec

2.1 Introduction

Involute gears, which transmit power through convex-convex contact, are used in contemporary machines almost without a competition. This is due to gradual development of *Euler's* [1] invention over centuries and important improvements in both manufacturing technologies and materials. This reflects in higher quality and loading capacity. However, the intrinsic property of the involute gear is its curvature radii function that is approaching to exceedingly small values in the dedendum part when approaching the base circle, where the said radius becomes zero. Therefore, high contact loads arise in this area. Additionally, for gears with a low number of teeth, the dedendum flank is comparatively short, thus invoking excessive sliding and friction losses and the possibility of premature damage in this area. Yet another problem is undercutting of the dedendum area. Therefore, there exists a permanent need for improved gears, with such features as a convex-concave contact, a stronger root, improved curvature radii, better lubrication conditions, etc. And S-gear geometry is an attempt in this context.

Many papers discussed various aspects of S-gears, e.g., their definition [2], possibilities of various gear types (e.g., helical, crossed, worm gears, planetary gears, etc.) [3], their radii of curvature, contact pressure, relative and sliding velocities, oil thickness, initial pressure angles, etc. [4–6], thermal properties [7], and various gearing aspects as well toward miniaturization or heavy industry. This

---

G. Hlebanja (✉)
University of Novo Mesto, Novo Mesto, Slovenia
e-mail: gorazd.hlebanja@siol.net

M. Erjavec · M. Hriberšek · L. Knez · S. Kulovec
Podkrižnik d.o.o., Nazarje, Slovenia
e-mail: miha.erjavec@podkriznik.si; matija.hribersek@podkriznik.si;
luka.knez@podkriznik.si; simon.kulovec@podkriznik.si

© Springer Nature Switzerland AG 2022

S. P. Radzevich (ed.), *Recent Advances in Gearing*,
https://doi.org/10.1007/978-3-030-64638-7_2

chapter discusses some shaping possibilities of external and internal gear pairs. Besides, an important issue—thermal properties and comparison to the involute gears – is presented in the chapter. This becomes of the utmost importance in plastic gears. Experiments with plastic gears confirm theoretically discussed properties.

2.1.1 Plastic Gears: Lifetime Testing

In the past decades, polymer materials for gears have been increasingly used. Polymer gears provide in many applications alternatives to traditional metal gears. The worldwide market for plastic gears in 2017 was estimated to be 2.67 billion € (3.06 billion US$); it will grow with a compound average growth rate (CAGR) of approximately 1.3% to 2.88 billion € (3.31 billion US$) in 2023. When polymer gears were entering the market in the second half of the twentieth century, they were predominantly used as cheap replacement for metal gears in simple applications. As designers and engineers have been constantly pushing the limits, polymer gears can in the meantime be found in a variety of power transmissions applications, including demanding high-performance uses in product with high added values.

Modern polymer gears have many benefits of their unique properties (e.g., lower specific weight, reduced moment of inertia, improved NVH performance—noise, vibration, harshness). Thermoplastic gears are mostly manufactured by injection molding process. Additionally, to achieve narrow tolerance requirements, in some cases they may also be made by hobbing.

Technical resins used for engineering purposes possess improved mechanical, electrical, and thermal characteristics compared to commodity plastics and are capable of withstanding complex loads in structurally demanding applications. The most common materials for gears are polyamide (PA), polyoxymethylene (POM), polyether ether ketone (PEEK), and polybutylene terephthalate (PBT). Additives are used sometimes to improve mechanical properties of polymer, e.g., glass, carbon, and aramid fibers. To decrease the temperature and consequently prolong lifetime, PTFE, silicon, graphite, and boron nitride can be used. Mechanical properties of plastics depend on material; however, production and test conditions also have influence. To predict mechanical stresses and consequently lifetime of gear pair, temperature-dependent material polymer materials must be modeled due to meshing process which is mechanically and thermally exposed phenomenon.

To determine the optimum material combination in terms of lifetime, temperatures, type of damage for appropriate gear application, the choice of materials for the driving, and the driven gear is crucial. Due to this fact, it is desirable to perform tests of polymer gears to determine behavior of chosen gear pair. The test can be accelerated with the aim to rapidly obtain suitability of meshed materials in terms of temperatures and wear. In order to optimize proper selection of a material, it is necessary to conduct lifetime tests under different loads with several repetitions for the same testing conditions. So, data cycles for thermoplastic gears are produced, which can be used for modeling a real gear pair for application in KISSsoft. Many researchers in the past used different material combinations, which have been proven as appropriate in the context of optimal operating lifetime, temperature distribution development (flank/tooth), and thermoplastic gear wear. According to the literature, the most used material combinations are Steel/POM, POM/PA, PA/PBT, and Steel/PA, sometimes in combination with various additives. S- and E-gears in a combination of driving alloy steel and driven POM gear lifetime tests are discussed in the chapter.

2.1.2 Planocentric Gearboxes with S-Gear Geometry

Planocentric gear boxes are in technical use for many decades due to their main characteristic, which is reduction of rotational speed and accordingly increased torque in the smallest available volume. The expected efficiency may be as high as 90% or more, and gear ratios can achieve up to 160:1 in a single step configuration. Basic arrangements of this type are described in renowned references, e.g., [8], and [9]. Gearboxes of this type are used in robotics, machine tools, aeronautics, aircraft, marine, and many other industries. The efficiency can be above 90%, and gear ratios can achieve up to 160:1 (160 rotations of the input shaft for a single turn of the output shaft). The available industrial solutions include *Sumitomo* cyclo gearboxes [10], *Spinea* drives [11], *Nabtesco* [12], *Onvio* [13], and many others. The device with the same function and different principle is Harmonic Drive. Gearings are usually cycloidal or lantern.

Pure mechanical drives can conform to high-tech industry requirements regarding backlash, lost motion, stiffness, hysteresis, etc. However, supplementary features based on sensorics can add additional functionalities to such gearbox. So, an accurate output shaft positioning and an output torque sensorics can be installed in the device as an option. Such new functionalities can enable incorporation of such devices in collaborative robot's arm joints and adaptive control. An upgrade to a self-aware condition monitoring system could increase the overall reliability of the drive and the effective predictive maintenance. And a corresponding condition monitoring could enable safe human interactions which is of special importance, e.g., in the field of robotics. Many analytical tools were used to analyze tolerances, to discover impact of some influencing factors like backlash, shaft deformation, and single or cumulative pitch deviation, and some of these methods are presented in the chapter.

2.2 S-Gears Geometrical and Thermal Properties

Some important properties of S-gears are the following:

1. Possibility of shaping by two parameters defining the rack flank curve, which can be used to modify teeth, e.g., a pressure angle, tooth thickness, etc.
2. Cylindrical spur S-gears can operate with a low number of teeth down to 6 or even 4.

3. Convex-concave contact in the vicinity of meshing start and end.
4. Comparatively lower radii of curvature, which implies lower contact pressure.
5. Higher contact oil film thickness, which is due to higher relative velocities in the contact.
6. S-gears exhibit relatively longer dedendum part of a pinion tooth flank (comparing to the involute gear) which is meshing with a gear addendum. Difference between the pinion dedendum length and the gear addendum length indicates amount of sliding. And less sliding means less frictional work and less developed heat, which is of special importance for plastic gears.

These properties are elaborated and compared to the involute gears. First, let us examine S-gear definition as illustrated in Fig. 2.1. To define a gear tooth flank, one needs to define a rack profile.

The rack profile with the coordinate origin in the kinematic pole is defined by the following function:

$$f(x) = \begin{cases} a_p m\left(1 - \left(1 - \frac{x}{m}\right)^n\right), & x \geq 0 \\ -a_p m\left(1 - \left(1 + \frac{x}{m}\right)^n\right), & x < 0 \end{cases} \tag{2.1}$$

where $\lim_{x \to 0^+} f'(x) = \lim_{x \to 0^-} f'(x)$.

Factors a_p and n, namely, the height factor and the exponent in Eq. (2.1), act as form factors, which affect the tooth shape properties. The initial pressure angle amounts to $\alpha_{w0} = 90° - \alpha_P(0)$ and $\alpha_P(0) = f'(0) = n\ a_p\ m$. So, the initial pressure angle is a dependent variable, $\alpha_{w0} = f(n, a_p)$, whereas the module m acts as a scaling factor. The rack tooth can be regarded as a cutting tool.

As illustrated in Fig. 2.1, the arbitrary point P_i on the rack tooth flank defines the unique point U_i on the path of contact. And this point U_i defines the point G_i on the tooth flank of a pinion and the point H_i on the tooth flank of a wheel, both with any number of teeth. This trigonometrical procedure, described in detail in [2], is valid for internal gear pairs as well. The transformations from the rack profile flank through the path of contact to gears are bijective, that is, they always give the same rack flank in the reverse direction. These transformations could also have been represented by object translations and rotations in appropriate coordinate systems, of course by employing the basic law of gearing.

As already stated, the gear flank and tooth shape influencing factors are a_p and n; however, one of them can be replaced by the initial pressure angle α_{w0}. Two gear pairs are shown here to illustrate the tooth shape variability, namely, the external (Fig.2.2) and the internal gear pair (Fig.2.3) with $z_p = 10$ and z_w or $z_r = 30$. Two gear pairs were designed: the first with $\alpha_w = 22°$ and $a_p = 1.3$ and the second one with $\alpha_w = 18°$ and $a_p = 1.5$ in both cases. All gears were designed with the module $m = 50$ mm, and since the module acts only as a scaling factor, its size is of no importance in this context. Rack profiles and paths of contact are the same for internal and external gears. Both rack profiles do not differ much, apart from the inclination and corresponding pressure angle. But the derived paths of contact

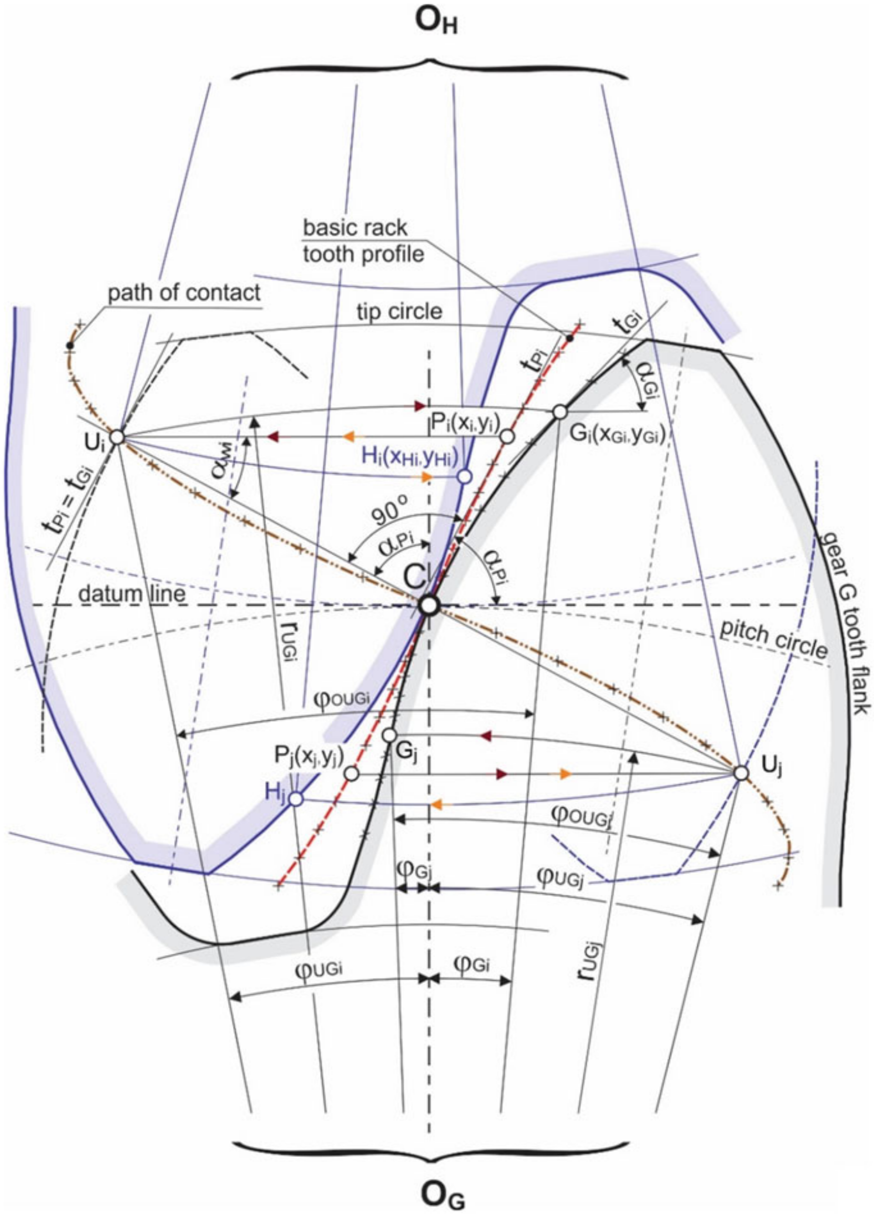

Fig. 2.1 Design of the path of contact, teeth flanks of both gears based on the rack profile [2]

apparently differ in their length and curvature in the meshing starting and end zones, as one can observe in Figs. 2.2 and 2.3. The active parts of both paths of contact delimited by gear tip circles are designated as $\widetilde{\mathbf{A}_1\mathbf{E}_1}$ and $\widetilde{\mathbf{A}_2\mathbf{E}_2}$. So, for the higher

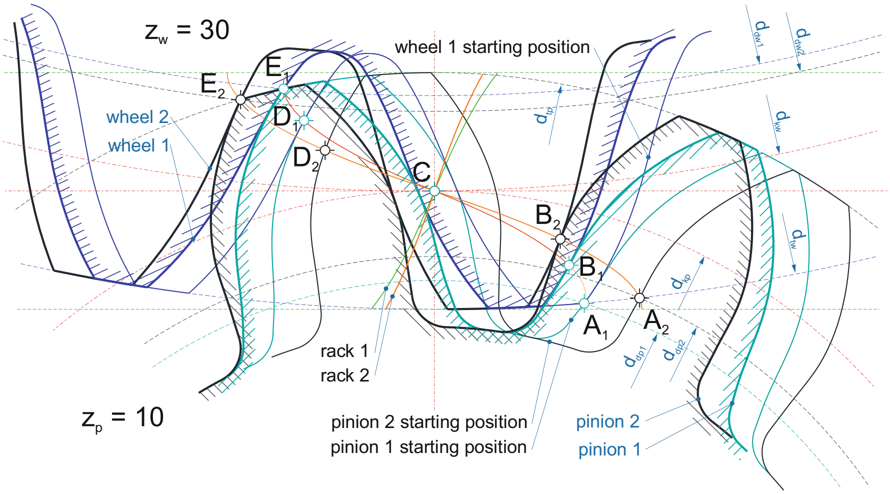

Fig. 2.2 External gear pairs with pinion $z_p = 10$ and wheel $z_w = 30$. The generating rack 1 with (initial) pressure angle $\alpha_w = 22^\circ$ and rack 2 with $\alpha_w 18^o$

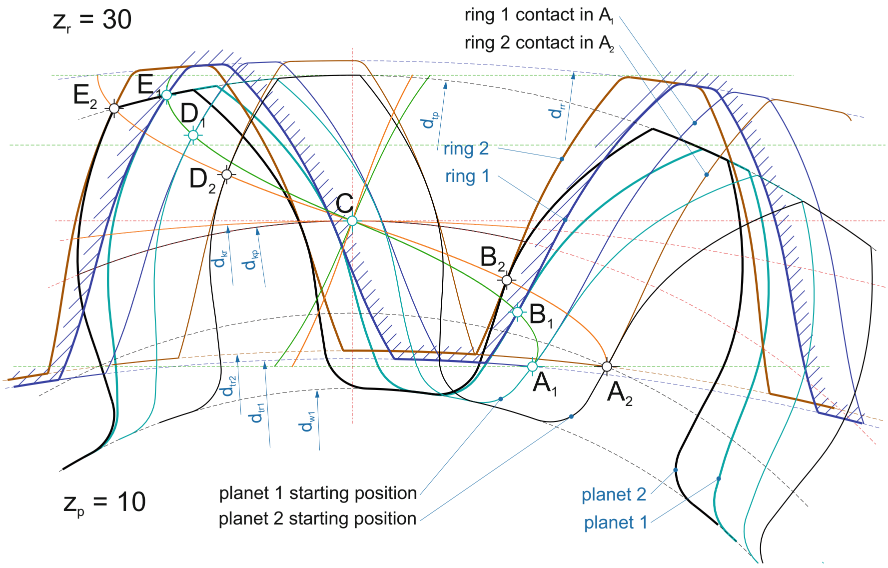

Fig. 2.3 Internal gear pairs with pinion $z_p = 10$ and wheel $z_w = 30$.The generating rack 1 with (initial) pressure angle $\alpha_w = 22^o$ and rack 2 with $\alpha_w 18^o$

pressure angle, the path of contact shortens and becomes more curved and inversely (longer and less curved path of contact) for lower pressure angles. The external tooth root becomes stronger and tooth tip thinner for the larger pressure angle and inversely for smaller pressure angles, whereas the internal gear tooth tip and tooth

Table 2.1 Path of contact characteristics for internal and external S-gear pairs ($z_p = 10$, $z_w = 30$, $m = 50$ mm)

Initial pressure angle α_{w0}	18	22
Internal gear pair		
Active length, $l_{\overset{\frown}{\mathbf{AE}}}$ [mm]	190.6	165.76
Base pitch, $l_{\overset{\frown}{\mathbf{AD}}}$ [mm]	150.4	145.6
Contact ratio, ε [/]	1.27	1.14
External gear pair		
Active length, $l_{\overset{\frown}{\mathrm{AE}}}$ [mm]	190.7	162.920
Base pitch, $l_{\overset{\frown}{\mathrm{AD}}}$ [mm]	148.2	144.5
Contact ratio, ε [/]	1.29	1.13

space at its root become thinner to some extent for higher pressure angles. And the internal gear addendum height shortens for lower pressure angles, as the meshing start points $\mathbf{A_1}$ and $\mathbf{A_2}$ show (Figs. 2.2 and 2.3). The active length of the path of contact $\overset{\frown}{\mathbf{AE}}$, the length $\overset{\frown}{\mathbf{AD}}$ which corresponds to the base pitch, and the contact ratio for all combinations from Figs. 2.2 and 2.3 are collected in Table 2.1.

A combination of internal and external S-gears can be used to design a planetary gear train, as the one illustrated in Fig. 2.4 [14]. It is true that the involute ring gear assures the concave contact in the entire contact zone, whereas the S-gears have a change to the convex-concave type of contact in the vicinity of the ring gear tip. So, the concave contact prevails. And more important, the planet and sun gear contacts are convex-concave, and gears with a small number of teeth can be designed.

2.2.1 Thermal Properties

Thermal load has a disadvantageous effect on the power transmission of a mating gear pair for all types of gears, regardless of size, material, or any other parameters. However, it is of a high importance in plastic gears due to their thermal sensitivity. Heat is generated by friction at the contacting surfaces of the mating teeth flanks where the load transmitting surfaces slide with the relative velocities. Work of friction depends on the flank load, the friction coefficient and on the sliding path length of a contact, whereas thermal power additionally depends on the sliding speed. The generated heat is treated as energy loss, where surface heating is unfavorable, and the temperature rise depends on heat flow into the gear material. Thermal properties of the employed gear material(s) are of the utmost importance in this context.

The mating gear teeth flanks combine the pinion dedendum and the gear addendum flanks from the meshing start to the kinematic pole C and the pinion addendum and the gear dedendum from C toward the meshing end point. The contact is propagating on the path of contact by rolling and sliding. The active size of the pinion dedendum is smaller than that of the gear addendum. This implies amount of sliding of the addendum on the shorter pinion dedendum, which is illustrated in

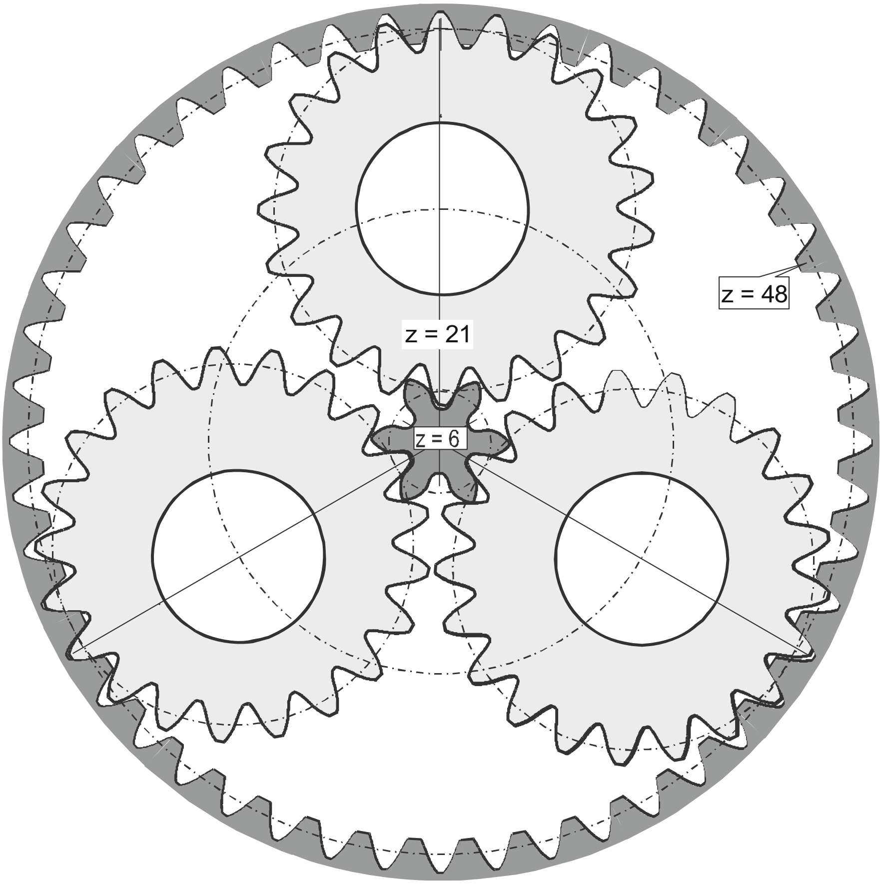

Fig. 2.4 A planetary (spur) gear train (sun gear z = 6, planet gear z = 21, ring gear z = 48)

Fig. 2.5 for both S- and E-gear pair. Amount of sliding also implies thermal impact. In general, the dedendum-addendum length difference depends on module, number of teeth, and pressure angle. For S-gears the said difference also depends on forming factors—the height factor a_p and the exponent n. The length difference in the case of S-gears is comparatively more convenient, so less sliding is produced along the contact propagation compared to the involute case. As Fig. 2.5. suggests:

$$\Delta l_\mathrm{E} = l\left(\widetilde{\mathbf{A}_\mathbf{ew}\mathbf{B}_\mathbf{ew}}\right) - l\left(\widetilde{\mathbf{A}_\mathbf{ep}\mathbf{B}_\mathbf{ep}}\right) > \Delta l_\mathrm{S} = l\left(\widetilde{\mathbf{A}_\mathbf{sw}\mathbf{B}_\mathbf{sw}}\right) - l\left(\widetilde{\mathbf{A}_\mathbf{sp}\mathbf{B}_\mathbf{sp}}\right) \tag{2.2}$$

Typical circumstances of the involute gears in the vicinity of the meshing start point disclose small driving pinion radii of curvature and rather high radii of curvature of the driven gear, which imply high sliding velocities in this area. The normal force F_N is transmitted through the contact, which causes the force of friction

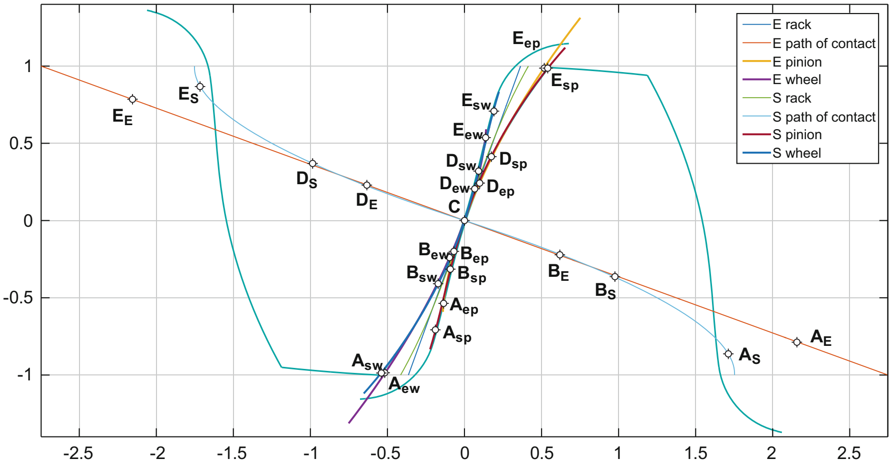

Fig. 2.5 Comparison of the E- and S-spur gear pair with $m = 1$ mm, $z_p = z_w = 20$, $\alpha_{wE} = 20^\circ$, and $\alpha_{wS} = 18^\circ$

F_{fr} oriented tangentially to the contact and the corresponding power of friction, $P_{fr} = F_{fr}\, v_g$. The power of friction being generated in the contact representing losses transforms to the heat flow, distributed to both involved flanks. A greater part of the heat is therefore distributed to the slower driving gear and the rest to the longer contacting area of the driven gear. The friction force grows to high levels already at the meshing start, which negatively influences (braking) the contact point velocity along the path of contact and induces negative sliding on the driving gear flank.

2.2.2 Analytical Approach

A program for calculation of the S-gear rack profile, the path of contact, the pinion, and the inner or outer gear was supplemented by necessary computations of power, work, flank pressure, contact width, velocities, and flash temperatures. All the parameters can be represented along the path of contact or the active flank profile. Power of friction is therefore given by:

$$P_{fr} = F_{fr} \cdot v_g = (\mu \cdot F_t / \cos \alpha_W) \cdot v_g \tag{2.3}$$

The work of friction along the active contact from $t_A = 0$ to t_E is given by the sum:

$$A_{fr} = \sum\nolimits_{tA}^{tE} P_{fri} \cdot \Delta t_i \tag{2.4}$$

So, the frictional work in a single pinion rotation is $z_p \cdot A_{fr}$ and multiplied by the rotational frequency frictional work accomplished in a minute $\nu \cdot z_G \cdot A_{fr}$. The

Table 2.2 Frictional work and average frictional power [7]

	S-gears	E-gears
$T_t = 0.6$ nm, $P_t = 90.415$ W, $\nu = 1439$ min^{-1}, $l_U = 3.891$ mm		
Work in a single contact	0.0052 J	0.0064 J
Work in a single rotation	0.1040 J	0.1278 J
Work in a minute	149.61 J	183,87 J
Average frictional power	2.4935 W	3.0644 W
$T_t = 0.7$ nm, $P_t = 104.8$ W, $\nu = 1428$ min^{-1}, $l_U = 4.5976$ mm		
Work in a single contact	0.0061 J	0.0075 J
Work in a single rotation	0.1213 J	0.1491 J
Work in a minute	173.21 J	212,87 J
Average frictional power	2.8868 W	3.5479 W

average frictional power is then $P_{fr\ av} = \nu \cdot z_G \cdot A_{fr}/60$. Table 2.2 collects data for the E- and S-spur gear pair with $m = 1$ mm, $z_p = z_w = 20$, $\alpha_{wE} = 20^o$, $\alpha_{wS} = 18°$, and b = 6 mm.

A calculation of flash temperatures was also conducted in [7]. Whereas the S-gear pair develop similar maximum values in A, B, D, and E, that is, approximately 38 K, the maximum values for the E-gear pair are in A and E and range around 59 K for the nominal load $T = 0.6$ Nm and $\nu = 1439$ min^{-1}.

2.3 Testing of Plastic Gears

Selection of material combinations for laboratory testing is based on the existing applications. Material alternatives were tested and characterized as well. Due to importance of proper material selection, the company decided to develop and produce own testbenches. Temperature measurements of a contact spot and temperature field of meshing gears were provided by a thermal camera. Optris Xi80 device was used for this purpose. Spot temperature was acquired during entire loading cycle of the lifetime tests, which was facilitated by Optris PIX Connect software. Based on test duration and rotational speed of the selected thermoplastic gears, lifetime cycles were calculated and imported together with flank/root temperature into Software KISSsoft (module Plastics Manager). Based on the processed input data in Plastics Manager, Wohler Curves (S-N) for selected material combinations were obtained. After each experimental lifetime test, the wear characterization has been performed according *VDI 2736* [15, 16] with Alicona device and evaluation of the gear failure mode.

2.3.1 Gear Geometry and Manufacturing

Small gears of equal size are used, with the module of 1 mm and z = 20. Some crucial differences between E- and S-gears were revealed in previous paragraphs. Important characteristics of these gears are collected in Table 2.3, whereas Fig. 2.6 shows the distinction between S- and E-geometry and two plastic materials.

Many manufacturing technologies were used in initial experiments, whereas material pair was a popular combination POM PA66. First, molded gears were employed, where it was discovered that shrinkage and corresponding coefficients can be unreliable and results elusive [17]. So, it was decided, that gears should be hobbed to reflect correct gear geometry, first with a single cutting hob. And

Table 2.3 Tested gear characteristics

Gear geometry	E	S
Teeth number, z [/]	20	20
Width, b [mm]	6	6
Module, m [mm]	1	1
Pressure angle at normal section, α [°]	20	18
Tip diameter, d_a[mm]	22	22
Reference diameter, d [mm]	20	20
Root diameter, d_f [mm]	17.5	17.7
Base diameter, d_b [mm]	18.79	–
Dedendum limit, d_{lm} [mm]	18.95	18.59
Base tangent length, W_k	7.66	

Fig. 2.6 Involute (above) and S-gears (below) made of PA66 (left) and POM-C (right)

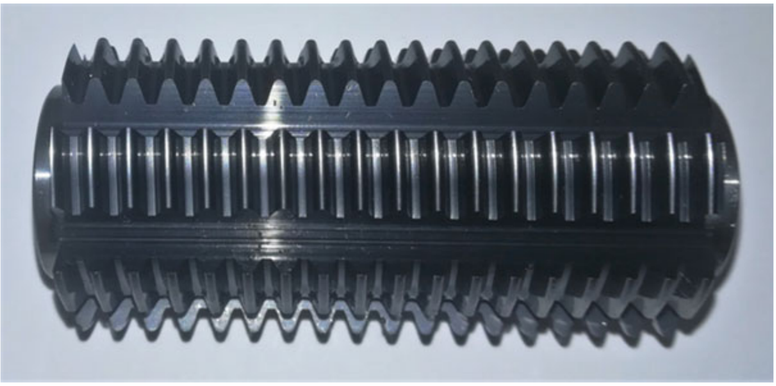

Fig. 2.7 S-gear hob for gears of module 1 mm

POM-PA66 raw material extruded rods. Since such operations are ineffective, regular hobs were produced for E- and S-gears (Fig. 2.7). Initially, raw parts are injection molded with the machine Krauss Maffei KM 50/100 CX. Raw parts were hobbed on Koepfer 200. Plastic parts are usually molded in general, whereas the expense for an injection tool could be too high for small lot sizes of a few thousand pieces. It was discovered [18] that the quality of molded gears compared to hobbed gears is at least two grades lower (measured with the 3D CMM Wenzel, with the gear inspection module). Inspection protocols according to DIN3961/62 revealed grade around Q8 for cut gears and above Q10 for molded gears. CMM is used regularly to ensure proper quality.

2.3.2 Testing Arrangement

Notable efforts in the promotion of a sustainable production lead toward more recycling and avoidance of harmful media. Therefore, lifetime tests are performed lubrication-free, i.e., dry on the own built testbenches in R&D laboratory of the Podkrižnik Company. The tests in discussion are conducted at ambient temperature. Figure 2.8 shows the testbench with a control and DAQ system.

The torque setting is based on a difference in the input values of frequency converters for a driving and a driven motor. The testbench calibration in terms of the selected torques was performed by measuring torsional deformations of a driving and a driven shaft at different setting frequencies.

During the entire duration of lifetime tests, spot temperatures and thermal state of meshing gears were measured with thermal camera Optris Xi80, where visualization was performed by PIX Connect software, as shown in Figs. 2.9a, 2.10a, and 2.11a. After each test, post-processing of time-temperature data was performed and aggregated. So, time-temperature diagrams were produced for the determined spot area of each meshing gear pair with S or E tooth flank profile. The prescribed conditions are

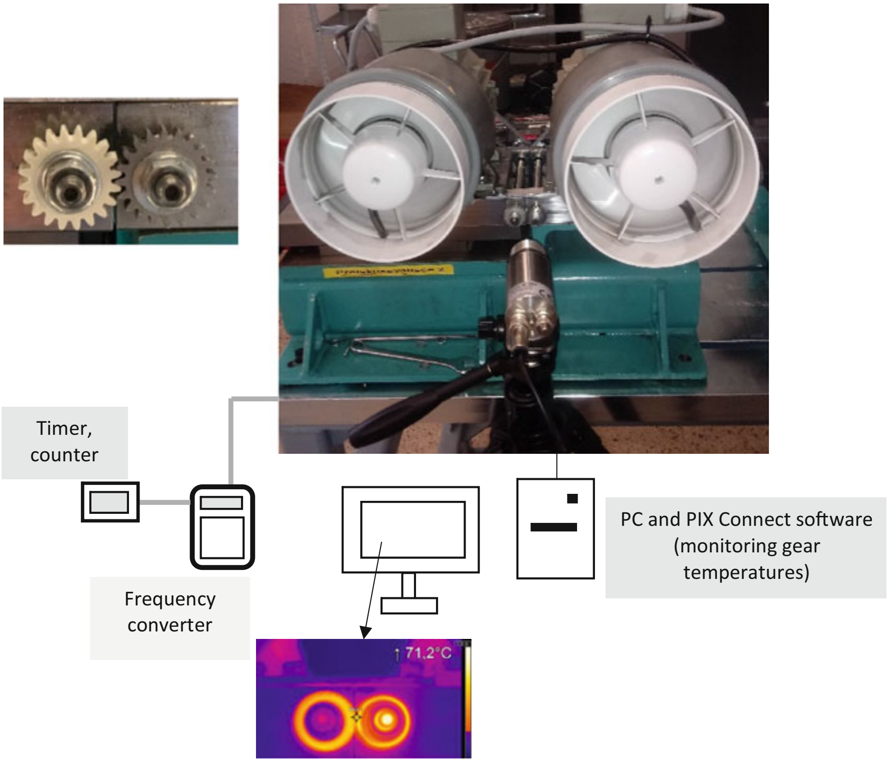

Fig. 2.8 Testing arrangement—testbench for lifetime testing of thermoplastic with thermal camera to monitor temperature data

presented in Table 2.4 and resulting temperature diagrams in Figs. 2.9b, 2.10b, and 2.11b.

Testbench is programmed to stop when a 5% decrease of input current of the motors and consequently torque decrease of the tested gear pair appear. A timer, which stops when the current drops due to gear failure, is connected to the frequency converters. The accurate test duration time is recorded in this way, and the duration time multiplied by RPM implies the number of cycles of the experiment.

In this series of experiments, a combination driving steel and driven POM gear was used. Torques leading to expediter lifetime characteristics were 1.5, 1.3, and 1.1 Nm. And a minimal statistical relevance was attained by three repetitions for each torque and both gear flank shapes. Lifetime tests were conducted at stable ambient laboratory temperature which was 22 °C ± 0.5 °C. The selection of torques was furthermore based on the preliminary lifetime testing of different types of polymer gears reported in [19].

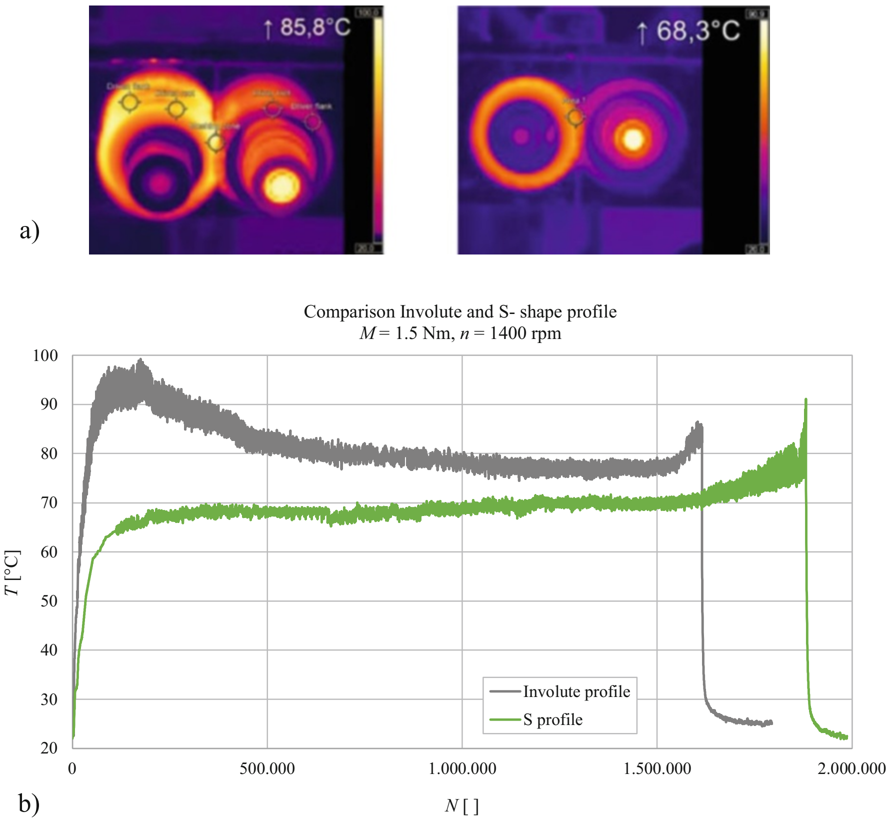

Fig. 2.9 Comparison of E- and S-tooth profile for a steel-POM gear pair at $M = 1.5$ Nm and $n = 1400\ \mathrm{min}^{-1}$. (**a**) Temperature spot in the meshing area E (left) and S (right) profile of teeth. (**b**) Temperature-time profiles (S, green; E, grey)

2.3.3 Experimental Results

The temperature-time dependency consists of three main sections, which are (a) running-in area where thermoplastic driven gear fits to steel gear in terms of tooth flanks; (b) a phase of a quasi-stationary operating at stable temperature; and (c) a phase of increasing gear wear that, in combination with fatigue, causes failure of thermoplastic gears.

The running-in phase of the E-gear pair has a characteristic course in the form of a transient phenomenon where the increase in temperature on tooth flanks was detected, which is due to the unmodified involute tooth tip profile, a high load, and subsequent teeth deformation (see [9], p. 98). So, a driven gear suffers an additional impact at a meshing start point A and temperature rise. The consequence is rather high initial wear of a driven plastic gear. S-gears do not exhibit such effects, so the temperature rise proceeds until the second, stationary phase.

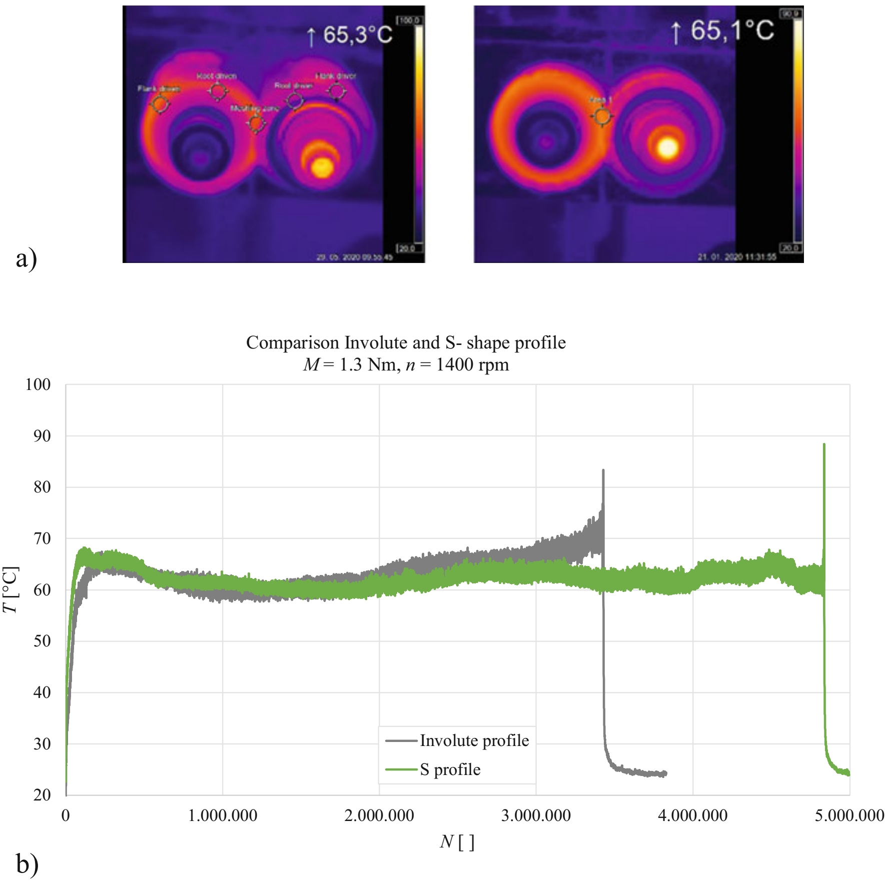

Fig. 2.10 Comparison of E- and S-tooth profile for a steel-POM gear pair at $M = 1.3$ Nm and $n = 1400\ \text{min}^{-1}$. (**a**) Temperature spot in the meshing area E (left) and S (right) profile of teeth. (**b**) Temperature-time profiles (S, green; E, grey)

In the next phase, relatively stationary conditions prevail. For E-gears the initially high temperature drops and prevails until the final phase. Uniform wear occurs in this phase for both gear types. The last phase of the lifetime test shows significant changes of the gears. This is due to the increased wear above the critical limit in connection with the fatigue of the material, which causes degradation of the bonds between the molecules in the material and the subsequent teeth failure.

The spot temperature for M = 1.5 Nm in the stationary zone is around 70 °C for S-gears and around 80 °C for E-gears. This temperature is in the zone above 60 °C for torque 1.3 Nm for both gear geometries. The E-gears do not show the abnormal temperature rise at start. However, S-gears have higher cycle numbers. The spot temperature for E-gears starts rising at about 2,000,000 cycles until final failure.

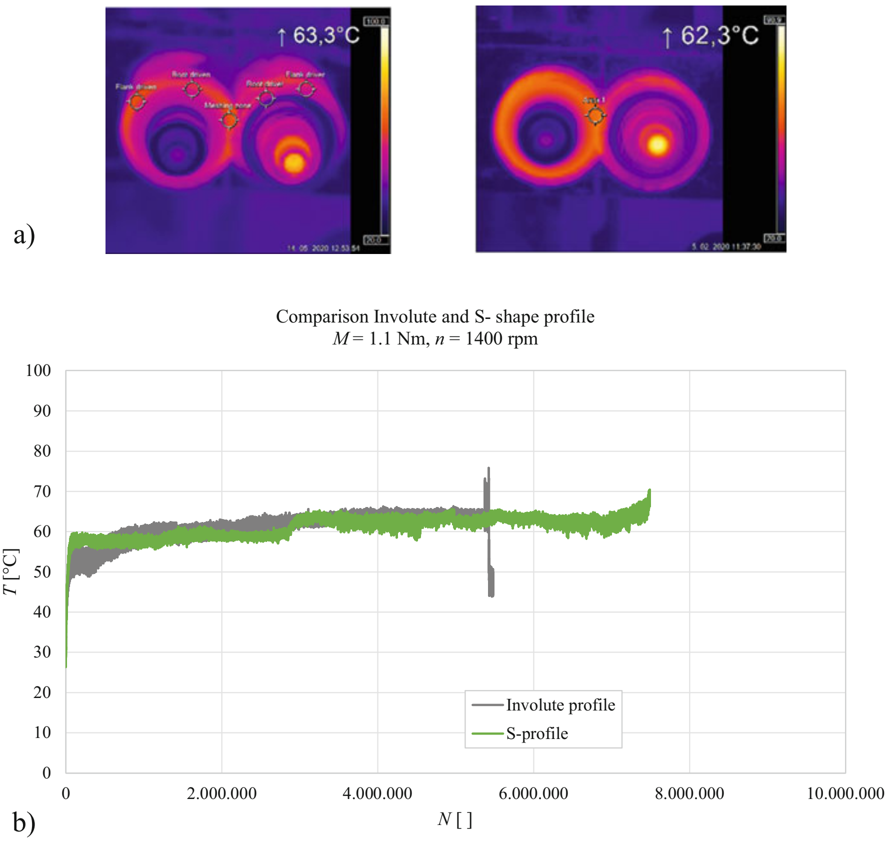

Fig. 2.11 Comparison of E- and S-tooth profile for a steel-POM gear pair at $M = 1.1$ Nm and $n = 1400$ min^{-1}. (**a**) Temperature spot in the meshing area E (left) and S (right) profile of teeth. (**b**) Temperature-time profiles (S, green; E, grey)

Table 2.4 Testing parameters at ambient temperature

INPUT PARAMETERS				
Gear pairing (driving gear-driven gear)	Tooth profile	Torque, M [Nm]	Rotational frequency of gears, n [min^{-1}]	Repetitons
Steel—POM	E- and S-shape	1.5	1400	3
Steel—POM	E- and S-shape	1.3	1400	3
Steel—POM	E- and S-shape	1.1	1400	3

The temperature-time diagrams for 1.1 Nm show similar temperature for both gear geometries, initially below and later above 60 °C without abrupt deviations during entire lifetime test for both gear types. However, there is a distinct difference

Table 2.5 Lifetime cycles of E- and S-gear pairs, driving gear steel, and driven gear POM

Load *M* [Nm]	E [$\times 10^6$]	S [$\times 10^6$]
1.5	1.62	1.88
1.3	3.43	4.84
1.1	5.34	7.83

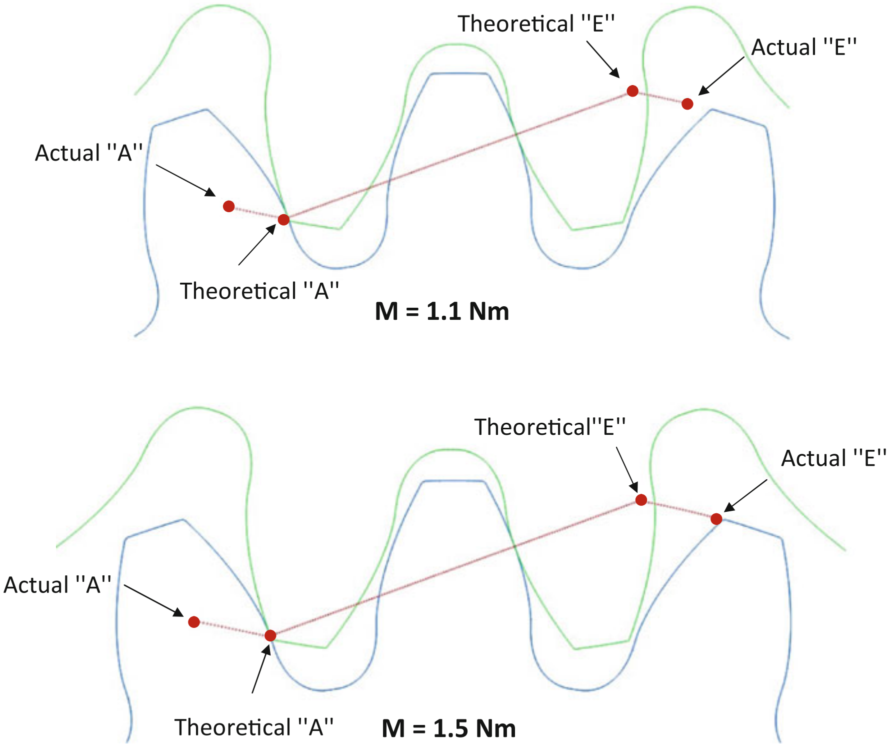

Fig. 2.12 Theoretical path of contact and actual meshing line (red) for 1.1 Nm (above) and 1.5 Nm (below) (driving steel gear, blue; driven POM gear, green)

in the number of loading cycles in favor of S-gears. The results are collected in Table 2.5.

The temperature behavior of E-gear pairs in the starting phase differs for higher and lower loads, which was numerically simulated for loads of 1.5 and 1.1 Nm. The contact analysis of meshing gears was provided by KISSsoft. Figure 2.12 shows results of the simulation for both loads for involute gear pair without tip relief.

The contact analysis for 1.1 Nm shows a transverse overlap ratio $\varepsilon_\alpha = 1.905$, meanwhile the theoretical one is 1.534. The increase of 24% in the transverse overlap ratio is clearly visible through distinctively prolonged part at the start, before point "A," and at the end, after point "E," of a meshing gear pair.

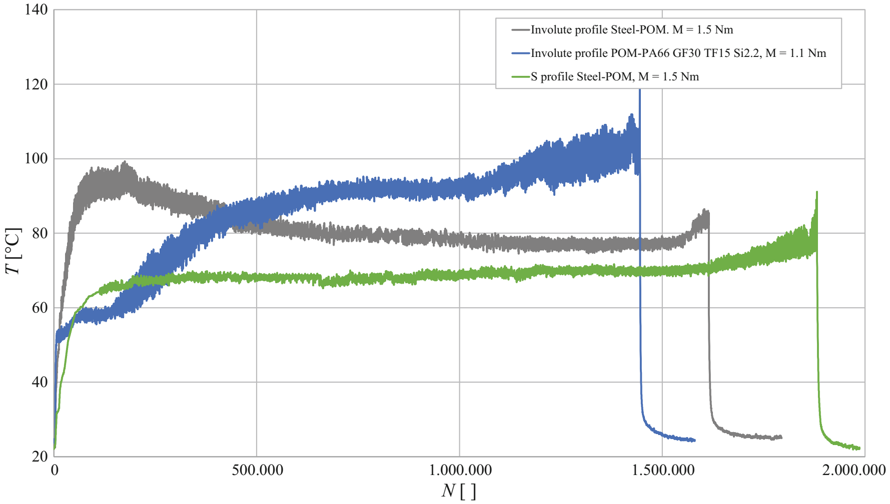

Fig. 2.13 Comparison of temperature-time diagrams for E- and S-gears for 1.5 Nm and E-gear pair with a POM-PA66 combination at 1.1 Nm—blue

For a higher load, 1.5 Nm, a transverse overlap ratio $\varepsilon_\alpha = 2.000$ is reported, which means the increase of 30% comparing to the theoretical one. The gears remain in mesh/contact for a longer time, hence producing more heat (out of roll—point "E"—location) due to higher teeth deformation which occurred at loading conditions M = 1.5 Nm compared to M = 1.1 Nm. It is assumed that the detected temperature distinction (Fig. 2.9b, E-gear shape) is due to unmodified tooth flank profile which induces increased wear of a POM gear driven by a steel gear.

The phenomenon of temperature increase for E-gear pairs with higher loads and material combination steel-POM (where POM is highly deformable) is typical for the said material combination, whereas two plastic materials tend to possess similar deformability. So, a combination of POM PA66 E-gear pairs when loaded with 1.5 Nm reveals continuous temperature rise to the short lifetime (around 200,000 cycles) with thermal failure. Figure 2.13 therefore shows POM-PA66 GF30 TF15 Si2–2 E-gears loaded by 1.1 Nm, compared to 1.5 Nm steel-POM combination (E- and S-gears). The temperature-time diagram for plastic gears shows different thermal behavior than steel-POM combination. Typically for the initial part of the lifetime test is that the temperature increases slowly due to uniform deformation of driver and driven gear for which thermo-mechanical properties are at the same level in terms of values. After the rise to around 60 °C, the temperature significantly increases again due to the drop in mechanical properties, especially Young Modulus *E* for both thermoplastics. This results in a higher deformation level and consequently higher temperatures generated in the meshing zone which imply higher wear of the gear tooth flanks. The increased wear rate in this case is also caused by fibers which can be on the surface of a hobbed gear. Temperature stabilization is conditioned by the achieved wear of the tooth flanks. When fatigue of material in combination with wear becomes critical, the failure occurs.

2.3.4 Wear Detection

The basic idea is to detect a shape of worn plastic gear and compare it to the new one. Such an analysis is facilitated by an optical 3D measurement microscope, Alicona Infinitive Focus SL. Some preliminary results for POM S-gear is presented below. So, the new S-gear is compared to a gear loaded by 1.1 Nm and failed after 7.851 x 10^6 cycles, which is illustrated for both gears in Fig. 2.14. Both profiles are compared in Fig. 2.15, where one can observe that the worn gear suffered severe wear and some plastic deformation before it failed. It seems reasonable to expect less wear with higher loads and lesser number of cycles.

2.4 Planocentric Gearbox with S-Gear Geometry

The planocentric gearbox has coaxial input and output shafts, and large transmission ratios can be achieved based on a gear ring with internal gearing in combination with usually two planet gears with external gearing, where the difference in the numbers of teeth between the gear ring z_v and the planet gears z_p rules the output gear ratio (Eq. 2.5). The difference in ring and planet numbers of teeth should be one, to achieve maximal reduction:

$$i_{out} = \frac{z_p - z_v}{z_p} \tag{2.5}$$

The planet gears are mounted on an eccentric shaft, where bearings separate the planet gears from the eccentric. The planet gears wobble around the gear ring, that is, they reverse for one tooth in each revolution of the eccentric. The wobbling movement is in accordance with a hypocycloidal movement where the generating circle with the radius of the eccentric is rolling on the kinematic circle of the ring gear. At the same time, the planet gear kinematic circle rolls in the inner side of the ring gear kinematic circle, which is simultaneous with the rotation of the eccentric. In this way the planetary gears develop rotation superimposed on the wobble. So, the input rotation of the eccentric is transformed into the reduced output rotation of the cage with the pins according to the gear ratio in the reverse direction of the input shaft in the same axis. And the gear ring is fixed to the housing.

SGU gearbox presented in this chapter is midsized device with $z_p = 80$ and $z_r = 81$ with reduction ratio 80 and nominal torque 120 Nm and backlash below 0.016^o.

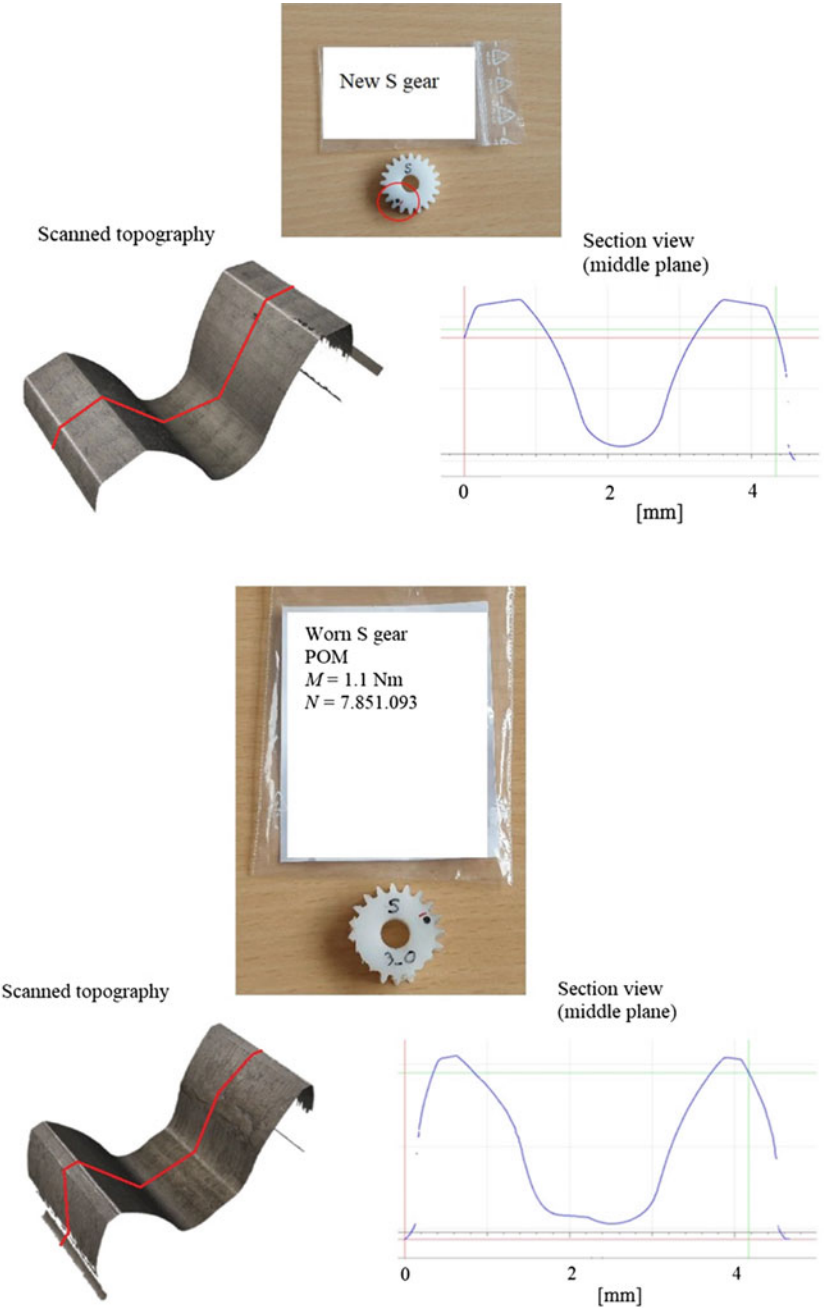

Fig. 2.14 3D scanned topography and 2D view of new (above) and worn (below) POM S-gear

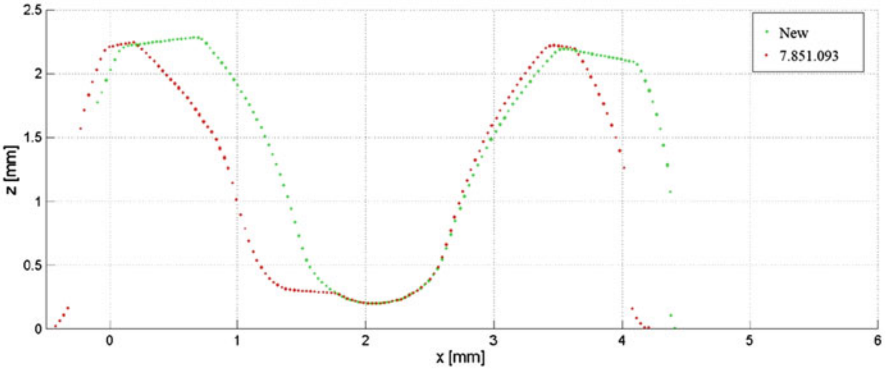

Fig. 2.15 2D wear presentation of S-gear at prescribed loading parameters: M = 1.5 Nm, n = 1400 min^{-1} at ambient temperature (red) compared to a new S-gear (green)

2.4.1 Kinematic Circumstances

The eccentric driven planocentric gear train can be regarded as a simple mechanism with two links. The first link size is the radius of the eccentric, and its joint indicates its position. The second one connects the eccentric with a point on the planet gear (a rigid body), e.g., the contact point. The eccentric link rotates and induces movement of the chosen point on the planet gear, which is restricted by the following rule:

$$r_v = r_p \frac{\varphi_p}{\varphi_v} \tag{2.6}$$

r_v and r_p are the radii of the kinematic circles of the ring gear and the planet gear, respectively. If the ring gear rotates for φ_v, the planet rotates for φ_p. Figure 2.16 illustrates movement of the planet based on the rotation of the eccentric and rolling of the planet kinematic circle on the fixed ring circle.

A simple algorithm can be used to define movement of the planet based on the rotation of the eccentric and limited by Eq. (2.6):

- $\mathrm{T_{p0}}$ and $\mathrm{T_{v0}}$ coincide with C. $\mathrm{P_0}$ is a point on the planet also coinciding with C.
- $\mathrm{T_{p1}}$ and $\mathrm{T_{v1}}$ are calculated according to Eq. (2.6). It is true: $p = \pi\, m = \widehat{CT}_{\mathrm{v1}} = \widehat{CT}_{\mathrm{p1}}$.
- Eccentric turns for φ_v to the new point $\mathrm{O_{p1}}$. kkp rolls on kkv in such a way that $\mathrm{T_{p1}}$ coincides with $\mathrm{T_{v1}}$. So, tangents and normals of kkv and kkp coincide in $\mathrm{T_{v1}}$.
- The normal of the planet in this point runs through $\mathrm{O_v}$ and $\mathrm{O_{p1}}$.
- Since the planet is a rigid body, the right leg of the angle φ_p rotates around $\mathrm{O_{p1}}$ in CW direction for the difference $\Delta\varphi = \varphi_v - \varphi_p$.
- The procedure is continuous, but it can be numerically calculated by any adequate number of steps.

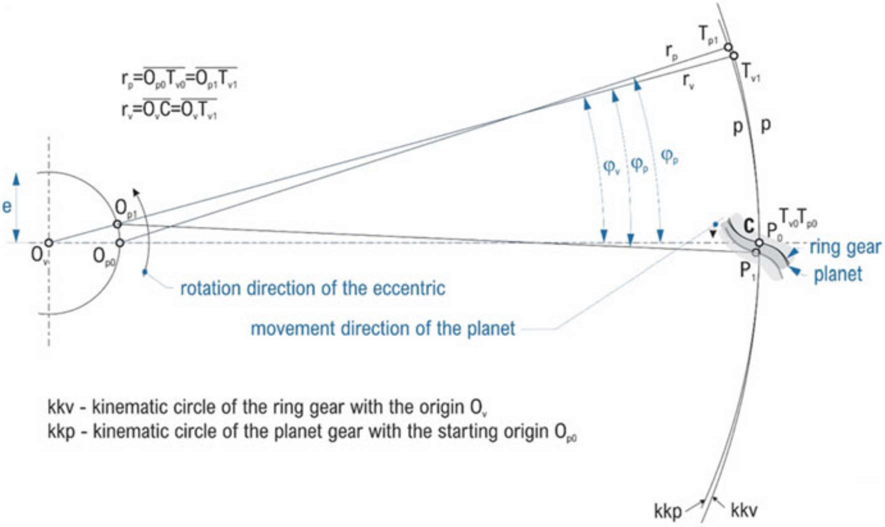

Fig. 2.16 Planetary gear movement as a simple mechanism with two links of the ring gear [14]

The above procedure can be formalized. Thus, successive points on the ring gear kinematic circle T_{vi} are defined as follows:

$$x_{Tvi} = r_v \cos\varphi_{vi} \quad \text{and} \quad y_{Tvi} = r_v \sin\varphi_{vi}. \tag{2.7}$$

Similarly, successive position points O_{pi} of the eccentric are:

$$x_{Opi} = e \cos\varphi_{vi} \quad \text{and} \quad y_{Opi} = e \sin\varphi_{vi}. \tag{2.8}$$

The coordinates of the moving point P_i on the planet gear are:

$$x_{Pi} = x_{Opi} + r_p \cos\Delta\varphi_i \quad \text{and} \quad x_{Pi} = y_{Opi} + r_p \sin\Delta\varphi_i. \tag{2.9}$$

The eccentricity e is defined by Eq. (2.10):

$$e = \frac{z_v - z_p}{2} \cdot m \tag{2.10}$$

The planet gear tooth movement into a new ring gear tooth space is illustrated in Fig. 2.17 by 20 iterations. So, each point and the planet gear position in Fig. 2.16 are based on successive rotations of the eccentric for 18°.

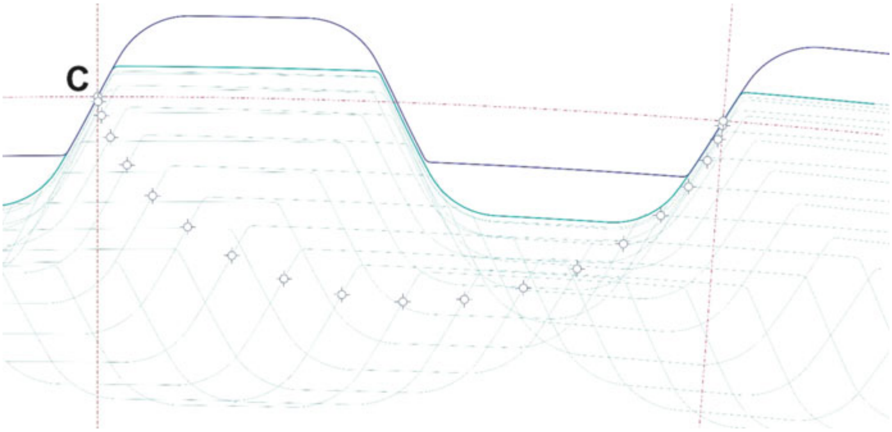

Fig. 2.17 Simulation of a planet gear tooth movement in accordance with hypocycloid generated on the kinematic circle of the ring gear [20]

2.4.2 Gradual Development

Several prototypes, named SGU, were produced, assembled, and tested during the development period. These prototypes were used for testing important characteristics and to acquire knowledge in design of succeeding gearbox. The gearbox contains an input shaft with eccentrics. As a motor rotates, the eccentric shaft rotates two planetary gears which wobble on the ring gear. Two planetary gears are positioned to enclose 180°. A cage consists of a supporting ring and output ring (serving also as the output shaft) that are connected by pins in an interference fit. The cage is rotated by planetary gears, having appropriate holes in which connecting pins with bearings comply. The cage is fixed to the input shaft by bearings at the extremities and in a similar manner to the housing with the ring gear. In this way a compact low-volume gearbox is designed. Initial prototypes are devices with a reduction ratio of 80 ($z_v = 81$ and $z_p = 80$), an outer diameter of around ϕ100, and having a module of 1 mm. The required maximal working torque is 120 Nm.

The device is presented in Fig. 2.18 with a 3D schematic and a photo. This gearbox incorporates an absolute output position encoder, which is also an innovative Slovenian product, namely, the *AksIM absolute rotary encoder* [21] made by RLS.

Crucial components, namely, the eccentric, the ring gear, and the planets are measured on a CMM before assembly. The tests include backlash, hysteresis and stiffness, kinematic error, vibrations, and noise, as well as durability tests. The devices were disassembled afterward, and critical components were inspected on the CMM and optically.

Figure 2.19 shows the ring gear and one of the planets of the specimen 01 after the conducted durability tests. The hole in the planet (which is adapted for the cage of pins with bearing bushings) is slightly worn in the circumferential direction

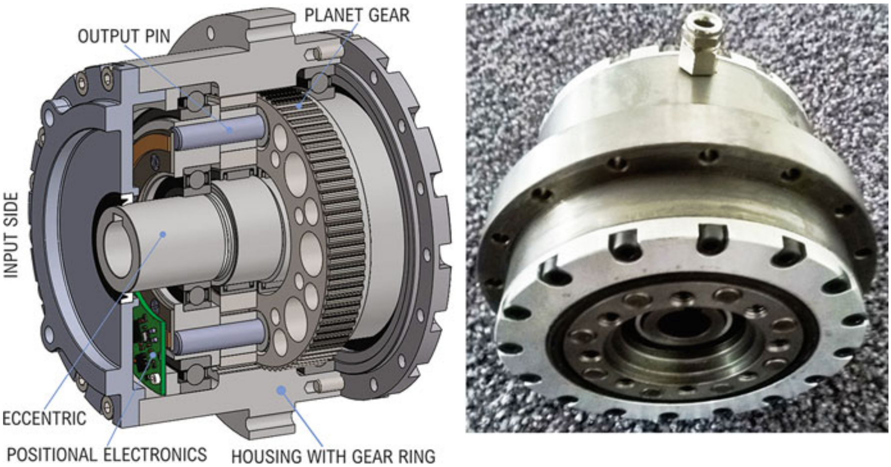

Fig. 2.18 3D schematics of the planocentic gearbox (left) and a prototype (right)

Fig. 2.19 Ring gear (left) and a planet (right) of a specimen 01 after durability tests

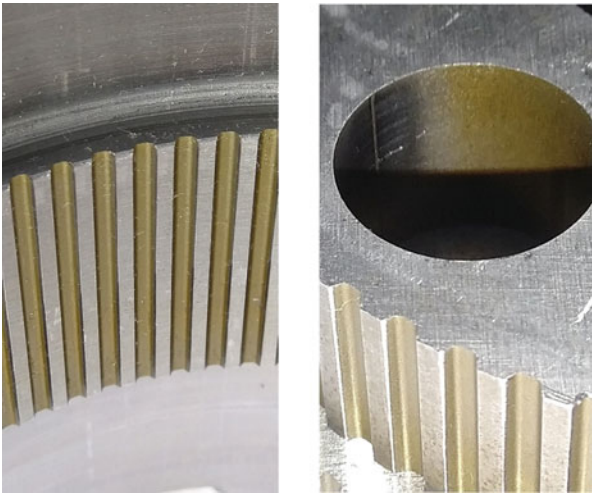

according to the acting force on the output bearing bushings of the pins. The specimen was submitted to high torques and speeds. The planet gears were made of 42CrMo4 and the ring of 25CrMo4, all gears plasma nitrided to HV700. The gears were also carefully examined by an optical microscope. The gear teeth did not show any wear or damages. Initial wear appeared in some planet teeth tips and at certain locations in teeth tips. The reason is in the meshing errors, which were discovered by measuring teeth of the planets and the ring gear with a CMM.

2.4.3 Backlash and Stiffness

The results presented in following paragraphs were done on a custom-built testbench, which was primarily used to conduct lifetime tests. The testbench is shown in Fig.2.20 and consists of two servo motors (SM), one on the input and one on the output side and a flange, which is used to attach the gearbox under test. SM1 drives the gearbox, and SM2 provides the torque load on the gearbox by breaking. The system is controlled by a PLC and uses the input and output torque sensors (both Kistler type 4520A200) and a hall sensor on the input side. Individual components of the system are connected by elastic couplings.

When needed the testbench was also upgraded with the Dewesoft, Dewe43A DAQ, system and the appropriate sensors for different tests. The obtained data was post-processed using a specific program written in Python. Two different types of tests are further presented in this manuscript:

- Measurement of the gearbox stiffness and backlash.
- Measurement of kinematic error.

The testbench described above in combination with the Dewesoft DAQ was adapted to measure the stiffness curves of the SGU gearbox as well as those of other robot gearboxes commercially available (labeled Drive 1 and Drive 2). For this purpose, the output shaft was fitted with the Renishaw incremental encoder (consisting of RESM20USA052 encoder ring and the reading head V2CKD20D20F). The torque was measured by the already mentioned Kistler torque sensor where the data acquisition (DAQ) rate was 20 kHz. The input shaft was held

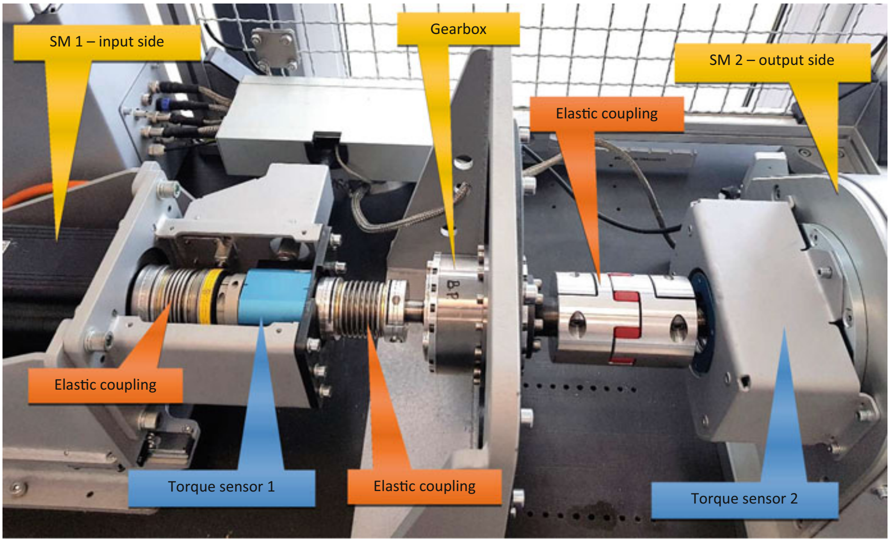

Fig. 2.20 Testbench used for lifetime tests (detailed view)

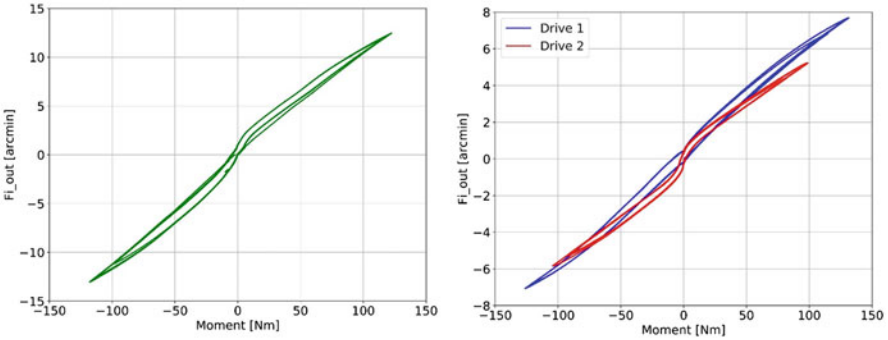

Fig. 2.21 Stiffness curve of the SGU gearbox (left) and commercially available gearboxes (right)

fixed by a clamp, and the output shaft was subjected to a torque load from approximately −130 Nm to 130 Nm by hand via a lever, which was purposely mounted at the output side of the testbench. The loading cycle was repeated three times as can be observed from Fig.2.21 (left). The curve actually represents the characteristic of the discussed planocentric gearbox. The resulting stiffness curves practically overlap, showing high repeatability of the measurement cycles. The stiffness curve is sectionally linear, and the backlash for the data in Fig. 2.21 is 0.89 arcmin (measured at 0 Nm).

It is interesting to compare the developed gearbox to other available high-tech devices. So, Fig. 2.21 (right) shows the stiffness curves of Drive 1 and Drive 2. A comparison with the SGU drive reveals approximately equal backlash values: Drive 1 0,9 arcmin and Drive 2 0,8 arcmin. The stiffness of these gearboxes however is higher, also sectionally linear.

To determine the overall or averaged backlash of the SGU gearbox, 36 different points were measured in the following manner:

- The first four points were obtained by sequentially rotating the input shaft by 90°.
- The input shaft was then rotated for 9x360°, and the next four points were then measured (90° apart).
- This pattern was repeated until the output shaft of the gearbox rotated for 360°, giving a total of 36 points (position of the first 4 points coincides with the last 4 points).

The result of each of the measuring points was a stiffness curve as shown in Fig. 2.21. From these curves, individual backlash values were determined, and the average value was the calculated. The individual backlash values and the average value for the SGU gearbox are shown in Fig. 2.22. The average backlash was 0.52 arcmin, whereas individual values would rise to 1 arcmin. The standard deviation of the measured data is 0.49 arcmin, which we believe can be attributed to geometric tolerances of different gearbox parts, especially the runout and single pitch deviation.

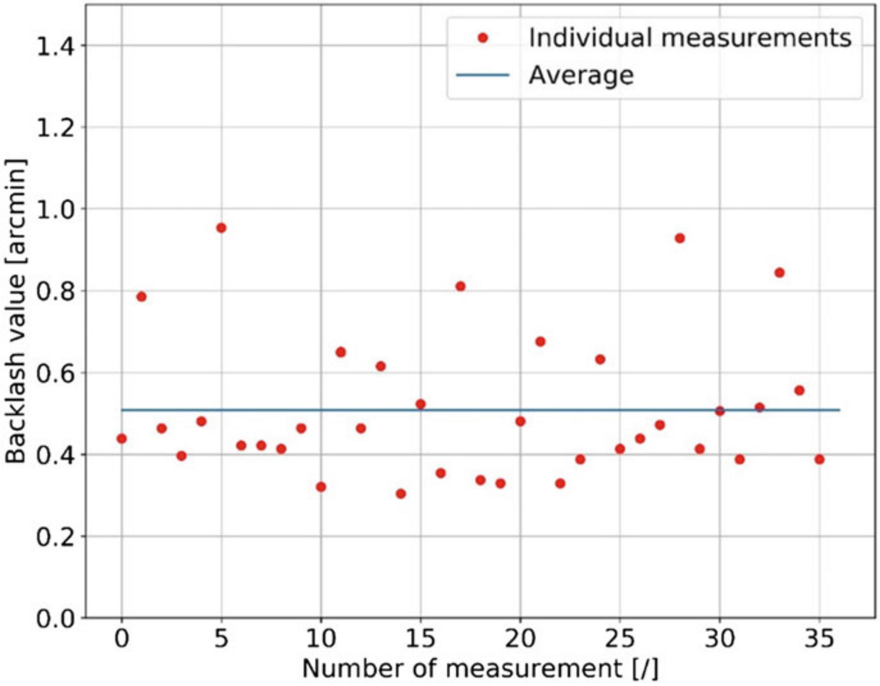

Fig. 2.22 Measured backlash values for 36 different points

2.4.4 Kinematic Error

The same testbench was also used to measure the kinematic error of the SGU gearbox. The measurements were done at a constant rotational speed. Two Renishaw incremental encoders were used on the input and output shaft to measure actual shaft positions. The ring RESM20USA075 and the reading head V2CLM20A20F was used on the input side, whereas the output side was equipped with the encoder ring RESM20USA052 and the reading head V2CKD20D20F. The acquisition speed of the DAQ was 200 kHz.

The kinematic error ($\Delta\varphi$) of a gearbox is the deviation of the angular position of the gearbox from its ideal, theoretical angular position. The kinematic error is measured as a difference between the input and output shaft rotation for full revolution (360°) of the output shaft, where the kinematic error is the difference between the maximal and minimal measured value. The kinematic error for SGU is:

$$\varphi_{out} + \Delta\varphi = i \cdot \varphi_{inp} \quad or \quad \Delta\varphi = i \cdot \varphi_{inp} - \varphi_{out} \tag{2.11}$$

The output ratio i is defined by Eq. 2.5. The incremental encoder (its scale), which is used to measure the rotation of the output shaft is always mounted with a small

Fig. 2.23 Eccentrically aligned encoder

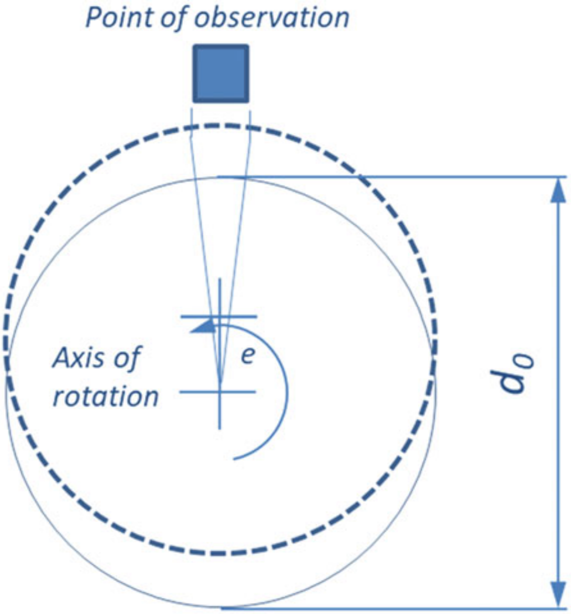

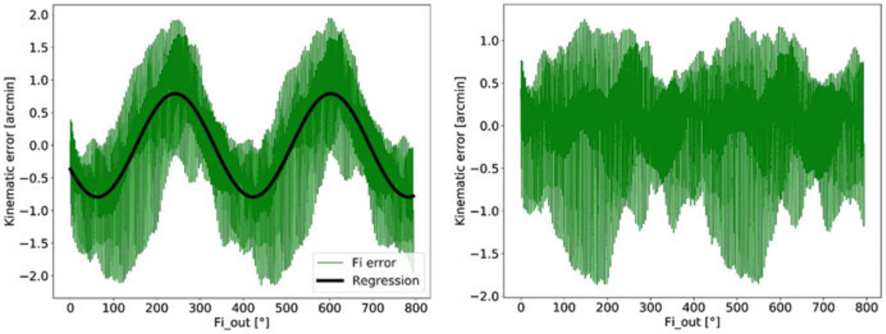

Fig. 2.24 Kinematic error of the SGU gearbox and the calculated regression line (left); the compensated kinematic error of the SGU gearbox (right); remark: vertical scale factors do not match

eccentric error as illustrated in Fig. 2.23. Consequently, the obtained measurements must be corrected with a regression curve [22]:

$$\frac{\Delta l}{\Delta \varphi} \approx r_0 + \boldsymbol{e} \cdot \cos\left(\boldsymbol{\varphi}_0 + \varphi\right) \tag{2.12}$$

r_0 is the scale radius, φ_0 the azimuth angle, e erroneous eccentricity, and φ phase angle.

The uncorrected (raw) results of the kinematic error measurements together with the fitted regression curve are presented in Fig. 2.24—left. And the corrected kinematic error of the SGU prototype, using the calculated regression curve is presented in Fig. 2.24—right. The kinematic error after correction, measured from a minimal to maximal value, is around 2.8 arcmin.

2.4.5 Influence of Geometric Tolerances

KISSsys and KISSsoft software [23] were employed to simulate and calculate various aspects of the SGU gearbox performance. However, the simulation of attainable manufacturing tolerances proved difficult; therefore, the gearbox kinematics was calculated using analytical equations, and a special program was written in Python. The input of the developed program is the nominal geometry, the rotation of the input shaft, the time vector, and the geometric tolerances (errors) of each of the gearbox components. The errors are user input and can be either measured from an actual component or obtained from the technical documentation of a future component.

The result of this program is an envelope of planet gear teeth movement into the ring gear tooth spaces, which is integrated in the gearbox housing. This result can be used to predict the gearbox backlash and a possible interference. An example of the calculated envelope for a chosen SGU tooth with the nominal geometry for the first three ring gear positions is shown in Fig. 2.25. As expected for the nominal geometry, the tooth fits optimally into the internal gear, resulting in a low (but not zero) backlash.

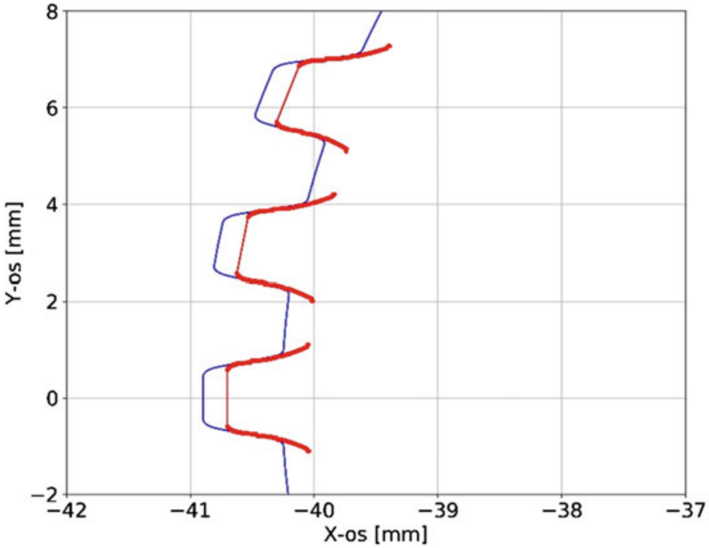

Fig. 2.25 Example of the kinematic envelope induced by a chosen planet gear tooth with nominal geometry into the first three spaces of the ring gear

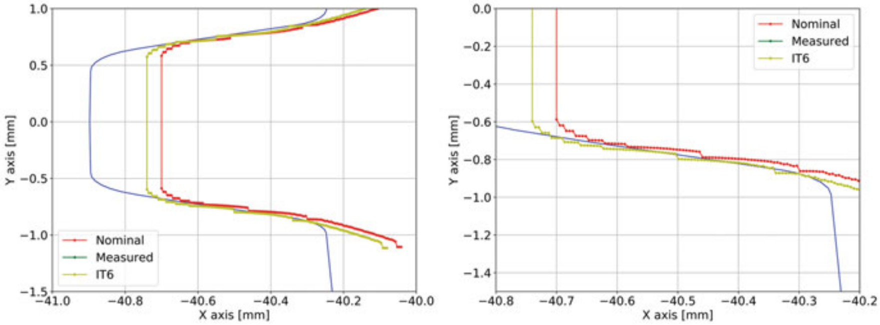

Fig. 2.26 Envelope of the SGU tooth in one of the internal gear slots; red, nominal geometry; green, measured tooth geometry; yellow, tolerances of IT6 and its detail (right)

Table 2.6 Input parameters used for the gearbox envelope calculation

Input	f_p [μm]	F_r [μm]
Nominal	0	0
Measured	10	40
IT6	7.5	20

Besides the nominal geometry, the program was used with various input parameters. A comparison between the nominal geometry, the measured geometry of an erroneous component, and the tolerance class IT6 geometry is presented in Fig. 2.26 (left) and zoomed to disclose some details in Fig. 2.26 (right). The input parameters used for the gearbox envelope calculation are shown in Table 2.6.

The nominal geometry fits ideally into the internal gear tooth spaces. However, the IT6 geometry is required by the technical documentation of the SGU gearbox and defined to produce a minimal (near zero or zero) backlash as presented in the results; the measured results are added as an example of a non-fit geometry. The latter are taken from measurements of erroneous components that proved difficult to turn in the assembled gearbox and based on measured values they correspond to IT9 tolerance class. The ragged edge of the envelope results from the way it is calculated:

- The geometry of a tooth (or teeth) is generated at first as a cloud of points.
- These points are then moved according to the appropriate kinematics and traced as they move, as it can be observed from Fig. 2.27.
- A search algorithm then finds the points that are on the outer edge (border) of movement. As a result, the ragged edge is generated.

Fig. 2.27 Movement of individual tooth profile points

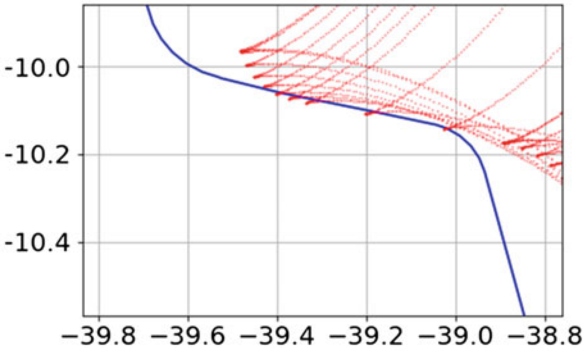

2.4.6 Single Pitch Deviation and Runout

Since the SGU gearbox should conform to requirements in high-tech industries, it is important to rule out also possible influences of the single pitch deviation f_p and runout F_r on the contact conditions of meshing gears. The definitions of the single pitch deviation and the runout are according to ISO1328-1 [24]. The simulation of the mesh conditions by the contact analysis considers influence of both parameters.

KISSsoft works with E-gears. However the current *KISSsoft* user manual [25] includes possibility of a progressive profile modification (p. 343 of the named manual), which can be used as a modification in the addendum and the dedendum of a gear tooth, and is defined as follows:

$$\Delta_{ad} = 2 \cdot C_{ad} \cdot \left(\frac{d - d_k}{d_t - d_k}\right)^{f_{ad}/5} \quad \text{and} \quad \Delta_{dd} = 2 \cdot C_{dd} \cdot \left(\frac{d - d_k}{d_v - d_k}\right)^{f_{dd}/5} \tag{2.13}$$

Δ_ad and Δ_dd stand for a profile modification function in addendum and dedendum. C_{ad} and C_{dd} are modifying tip relief (or corresponding active dedendum modification) and f_{ad} and f_{dd} power coefficients. If a coefficient amounts to 5, the relief becomes linear. d_t, d_v, d_k, and d, are diameters of the tip circle, dedendum circle, kinematic circle, and current circle. One can adapt the involute flank addendum and dedendum to S-gear flank in this way. Such a modification is justified since the addendum and dedendum heights are rather small, between 0.2 and 0.25 m.

The simulation takes the tolerance allowance requirement form gear drawings corresponding to the quality class Q6 in accordance with ISO1328-1, i.e.,$f_\mathrm{p} = 7.5$ μm and $F_\mathrm{r} = 21$ μm for each gear, planet, and the ring gear.

Since eventually each tooth of a given gear will come in mesh with each tooth of its counterpart gear, a contribution of both pitch and runout deviations of both gears shall be considered. This is done by the quadratic tolerance sum, i.e., for the single pitch deviation f_p and for the runout F_r:

$$f_p = \sqrt{f_{p1}^2 + f_{p2}^2} \quad \text{and} \quad F_r = \sqrt{F_{r1}^2 + F_{r2}^2} \tag{2.14}$$

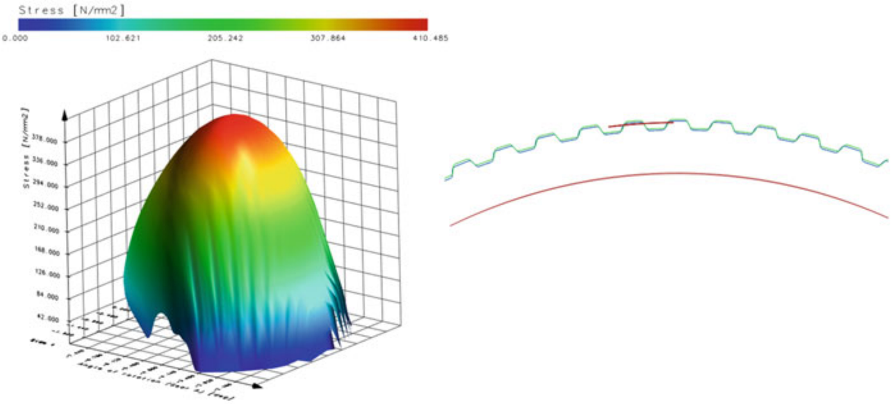

Fig. 2.28 Contact pressure (left) and mesh line at $f_p = +8.16$ µm and $F_r/2 = +11{,}425$ µm (right)

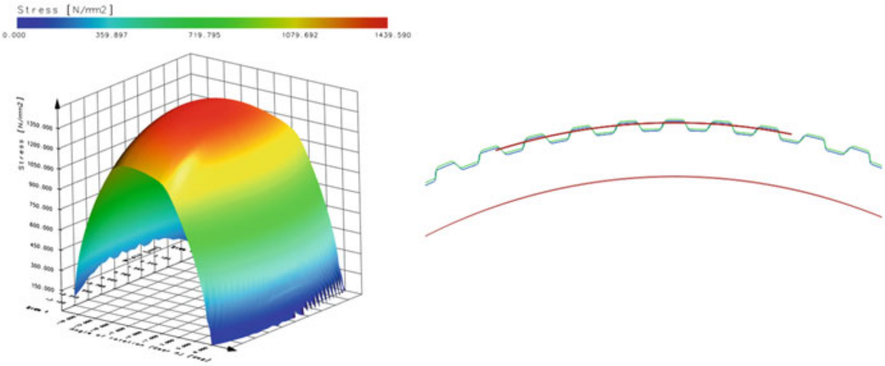

Fig. 2.29 Contact pressure (left) and mesh line at $f_p = -8.16$ µm and $F_r/2 = +11{,}425$ µm (right)

From the practical aspect, assuming the manufacturing process is stable, with $C_\mathrm{p} \geq 1.33$ (C_p is the process capability index), and considering the equations above, the values to be considered are $f_\mathrm{p} = 8.16$ µm and $F_\mathrm{r} = 22.85$ µm. Hence, the simulation parameters matrix consisting of four individual cases is defined:

1. $f_\mathrm{p} = \pm 8.16$ µm,
2. $F_r/2 = \pm 11{,}425$ µm.

Figure 2.28 (right) depicts the mesh line at $f_\mathrm{p} = +8.16$ µm and $F_\mathrm{r}/2 = +11{,}425$ µm, whereas Fig. 2.28 (left) illustrates the contact pressure of meshing gears. The transverse contact ratio is $\varepsilon_\alpha = 1.45$ and the contact pressure 410 MPa, if both simulation parameters are positive.

Figure 2.29 collects results if the single pitch deviation becomes negative. So, the contact pressure of meshing gears and the mesh line at $f_\mathrm{p} = -8.16$ µm and $F_\mathrm{r}/$

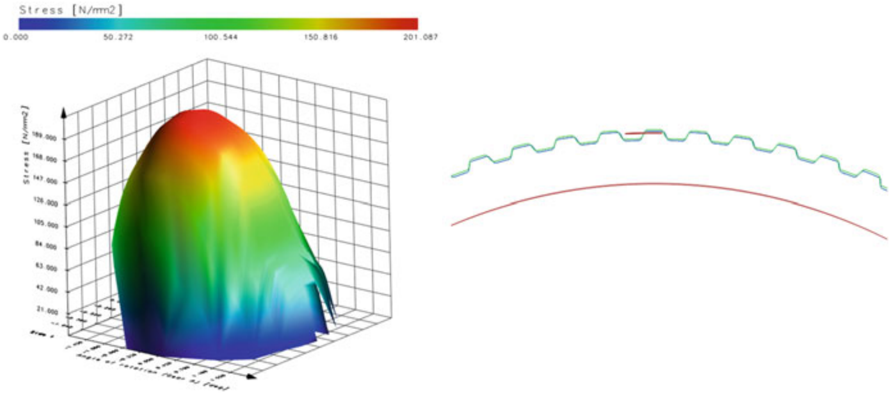

Fig. 2.30 Contact pressure (left) and mesh line at $f_p = +8.16$ μm and $F_r/2 = -11{,}425$ μm (right)

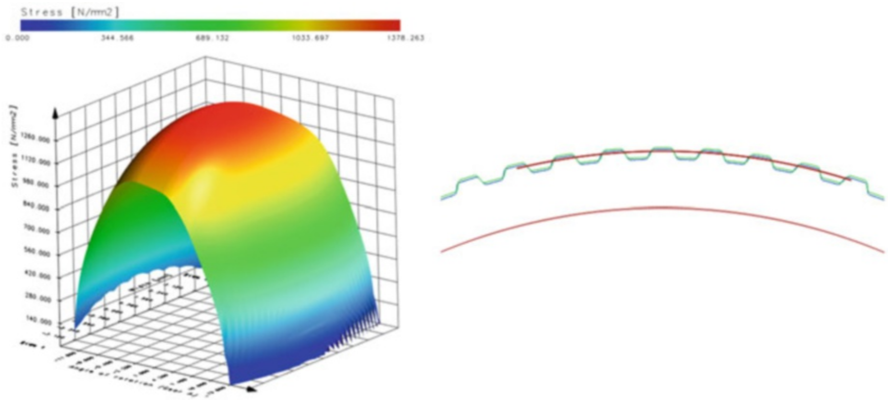

Fig. 2.31 Contact pressure (left) and mesh line at $f_p = -8.16$ μm and $F_r/2 = -11{,}425$ μm (right)

2 = +11,425 μm are presented. The transverse contact ratio is $\varepsilon_\alpha = 6.37$ and the contact pressure 1440 MPa.

The next combination is for the positive single pitch deviation $f_p = +8.16$ μm and the negative runout $F_r/2 = -11{,}425$ μm and presented in Fig. 2.30. The transverse contact ratio is $\varepsilon_\alpha = 0.81$ and the contact pressure 201 MPa.

And finally, a simulation for both negative values is conducted, so the values for $f_p = -8.16$ μm and $F_r/2 = -11{,}425$ μm are considered in Fig. 2.31. The transverse contact ratio is $\varepsilon_\alpha = 6.85$ and the contact pressure 1378 MPa.

Additional simulations for evaluation of the single pitch deviation influence should be performed with the values for a single pitch deviation $f_p = \pm 8.16$ μm and without zero runout ($F_r = 0$ μm).

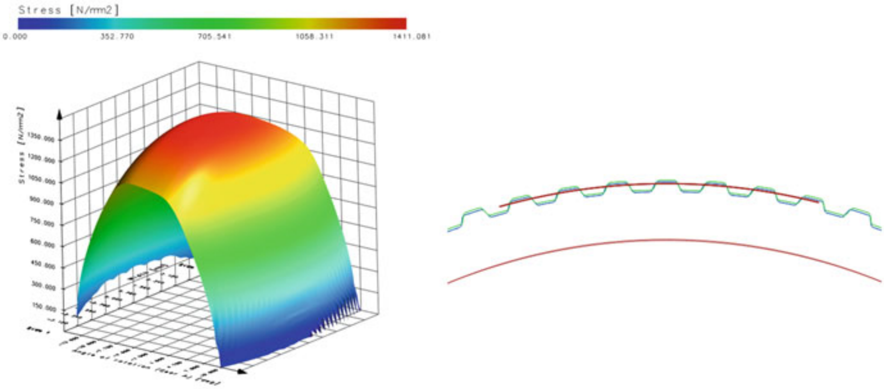

Fig. 2.32 Contact pressure (left) and mesh line at $f_p = -8.16$ µm and $F_r/2 = 0$ µm (right)

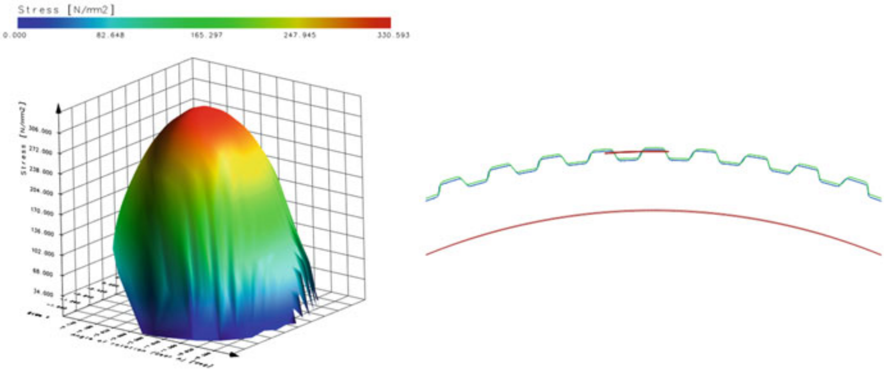

Fig. 2.33 Contact pressure (left) and mesh line at $f_p = +8.16$ µm and $F_r/2 = 0$ µm (right)

Two cases are possible, as shown in Fig. 2.32. with the negative $f_\mathrm{p} = -8.16$ µm and Fig. 2.33 with the positive $f_\mathrm{p} = +8.16$ µm. In the first case, the transverse contact ratio amounts to $\varepsilon_\alpha = 6.57$ and the contact pressure to 1411 MPa, and in the second case the transverse contact ratio amounts $\varepsilon_\alpha = 1.22$ and the contact pressure to 331 MPa.

The analysis shows that a single pitch deviation influences the meshing gears with a high impact. The runout itself is neglectable compared to the single pitch deviation. Therefore, a special care for a single pitch deviation should be taken when manufacturing gears which means the optimization of the manufacturing technology should focus on achieving best possible single pitch deviation, hence a better quality than Q6.

2.5 Conclusion

The presented chapter deals with S-gears, which are defined with a half parabolic function of the rack flank, which then defines a single path of contact, and this implies an external or internal gear geometry. Furthermore, the definition parameters a_p and n and the derived parameter—the initial pressure angle α_w in C facilitate shaping of the gear, which was demonstrated in the chapter. Thermal properties of S-gears, i.e., their advantage over E-gears are due to the fact that the former mesh with less sliding and more rolling, so S-gears reveal less frictional force and frictional losses or heat.

The next subchapter deals with lifetime testing of S- and E-gears. The examined gear pairs were a combination of an alloy steel driving gear and a driven POM gear (POM contained some heat-resistant additives). The tests with loads of 1.5, 1.3, and 1.1 Nm were repeated at least three times. They were conducted on small testbenches with thermal camera coverage and data logging. The testbench automatics registered failure time. There was a clear distinction between the S- and E-gears in favor of the former.

SGU planocentric gearbox is designed with S-gear geometry. The prototype series has a reduction ratio of 80; it already contained an absolute position encoder. And as an option, it can incorporate a torque sensor as well. The development question was how to assemble a device with proper performance and how to implement fast and accurate certification tests, e.g., backlash and stiffness curves, kinematic error, noise and vibration, durability tests, etc. That is why the testbench was designed and built, which helped in the assessment of many important results. The second part of the subchapter 2.4 is about analytical approach which also disclosed many development guidelines. So, it was analytically ascertained that gears should be put in (sub)tolerance ranges, and ring gears and planets should be mated (one in the higher subclass and the other in the lower one) [20], to attain better accuracy of the device. Also, the influence of the bearing and carrier tolerances was analyzed and discovered that even the robust device can deform to such extent that gear teeth can be in interference and tooth tips should be adapted. It was also found out that the single pitch deviation has a high impact on the gearbox operation, so a special care for a manufacturing process is necessary.

Acknowledgments The investment is co-financed by the Republic of Slovenia and the European Union under the European Regional Development Fund, no. SME 2/17-3/2017 and C3330-18-952014.

References

1. Euler, L. (1760). Novi Commentarii academiae scientiarum. *Petropolitanae, 5*(1760), 299–316.
2. Hlebanja, J., & Hlebanja, G. (2010). Spur gears with a curved path of contact for small gearing dimensions. In *International Conference on Gears, Garching near Munich, Germany, 4.-*

6.10.2010: Europe invites the world, (VDI-Berichte, ISSN 0083–5560, 2108) (pp. 1281–1294). Düsseldorf: VDI-Verlag.

3. Hlebanja, J., & Hlebanja, G. (2005). Anwendbarkeit der S-Verzahnung im Getriebebau: Nichtevolventische Verzahnungen weiterentwickelt. *Antriebstechnik.*, ISSN 0722–8546*, 44* (2), 34–38.
4. Hlebanja, G. (2011). Specially shaped spur gears: A step towards use in miniature mechatronic applications. In V. Miltenović (Ed.), *Proceedings, The 7th International Scientific Conference Research and Development of Mechanical Elements and Systems - IRMES 2011, 27.-28.4.2011* (pp. 475–480). Zlatibor: Mechanical Engineering Faculty.
5. Hlebanja, G., & Hlebanja, J. (2012). Recent development of non-involute cylindrical gears. In G. Dobre & M. R. Vladu (Eds.), *Power Transmissions: Proceedings of the 4th Int. Conf., Sinaia, Romania, June 20–23, 2012, (Mechanisms and machine science, ISSN 2211–0984, ISSN 2211–0992, Vol. 13)* (pp. 83–98). Dordrecht: Springer. 2013.
6. Hlebanja, G., & Hlebanja, J. (2013). Influence of axis distance variation on rotation transmission in S-gears: Example on heavy duty gears. In *International Conference on Gears, 7–9.10.2013, Garching (near Munich), Germany: Europe invites the world, (VDI-Berichte, ISSN 0083–5560, 2199)* (pp. 669–679). Düsseldorf: VDI-Verlag.
7. Hlebanja G, Kulovec S, Zorko D, Hlebanja J, Duhovnik J (2017). Influence of the tooth flank shape on thermal load of the gear. Europe invites the world, International Conference on Gears, International Conference on Gear Production, International Conference on High Performance Plastic Gears, Technische Universität München, Garching, Sept. 13–15, (VDI-Berichte, ISSN 0083–5560, 2294.2). Düsseldorf: VDI., p.p 1583–1592.
8. Radzevich, S. P. (2012). *Dudley's Handbook of Practical Gear Design and Manufacture, Second Edition*. Boca Raton: CRC Press, Taylor & Francis Group. ISBN 978–1–4398-6602-3 (eBook - PDF).
9. Nieman, G., & Winter, H. (1989). *Maschinenelemente, Band II: Getriebe allgemein, Zahnradgetriebe Grundlagen, Stirnrad Getriebe. ISBN 3-540-11149-2*. Berlin, Heidelberg, New York: Springer Verlag.
10. Sumitomo Drive Technologies (2018), F*ine Cyclo® - Zero Backlash Precision Gearboxes, Catalog #991333.* Accessed 01/07/2020, from www.sumitomodrive.com.
11. Spinea TwinSpin (2017) *High Precision Reduction Gears, Ed. I/*2017. Accessed 01/07/2020, from https://www.spinea.com/en/products/twinspin/index.
12. Nabtesco Precision Reduction Gear RV™ (2018). *E Series/C Series/Original Series CAT.180420*, Accessed 01/07/2020, from https://www.nabtesco.de/fileadmin/05_downloads/03_kataloge/produktkatalog_en.pdf
13. Onvio Zero Backlash Speed Reducers (2005), Accessed 01/07/2020, from www.onviollc.com
14. Hlebanja J, Hlebanja G (2009) Konkav-konvexe Sonderverzahnungen, Vorteile und Nachteile gegenüber Evolventenverzahnungen. Mihailidis A (Edt.). Proceedings, The 3rd Int. Conf. – Power Transmission '09 Kallithea, Greece, 1–2.10.2009. Thessaloniki: Sofia Publications. 2009, p. 21–26.
15. VDI 2736 (2016a) VDI 2736 - part 4. Thermoplastic gear wheels: Determination of strength parameters on gears. VDI–Richtlinien (2016).
16. VDI 2736 (2016b) VDI 2736 - part 1. Thermoplastic gear wheels: Materials, material selection, production methods, production tolerances, form design. VDI–Richtlinien (2016).
17. Hlebanja, G., Kulovec, S., Hlebanja, J., & Duhovnik, J. (2014). S-gears made of polymers. *Ventil, 20*(5), 358–367.
18. Hlebanja G, Hlebanja J (2018) S-gears: From Metal to Polymer Solution. Goldfarb V, Trubachev E, Barmina N (Edt.). Advanced Gear Engineering, (Mechanisms and machine science, ISSN 2211–0984, ISSN 2211–0992, Vol. 51). Cham: Springer Nature. 2020, p. 255–269, doi: https://doi.org/10.1007/978-3-319-60399-5_12.
19. Hlebanja, G., Hriberšek, M., Erjavec, M., & Kulovec, S. (2019). Durability investigation of plastic gears. In *Power transmissions 2019, 6th international BAPT conference power transmissions 2019, Varna, Bulgaria, June 19-22, 201, (MATEC web of conferences, ISSN 2261-236X, vol. 287)* (Vol. 287, pp. 1–9). Paris: EDP Sciences.

20. Hlebanja, G., Erjavec, M., Kulovec, S., & Hlebanja, J. (2020). Optimization of planocentric gear train characteristics with CA-tools: Chapter 14. In V. Goldfarb, E. Trubachev, & N. Barmina (Eds.), *New approaches to gear design and production, (Mechanisms and machine science, ISSN 2211–0984, ISSN 2211–0992, Vol. 81)* (pp. 323–347, https://link.springer.com/chapter/10.1007%2F978-3-030-34945-5_14). Cham: Springer Nature. https://doi.org/10.1007/978-3-030-34945-5_14.
21. AksIM 2 (2020) Absolute rotary encoder, datasheet, Accessed 15/06/2020, from https://www.rls.si/en/aksim-2-off-axis-rotary-absolute-encoder.
22. Renishaw (2020) The accuracy of rotary encoders (Whitepaper). Accessed 30/06/2020 from https://resources.renishaw.com/en/details/white-paper-the-accuracy-of-angle-encoders-113122.
23. KissSoft (2019a) *Design software for mechanical engineering applications*. Accessed 23/9/2019 from https://www.kisssoft.ag/english/home/index.php.
24. ISO1328-1 (2013). Cylindrical gears — ISO system of flank tolerance classification — Part 1: Definitions and allowable values of deviations relevant to flanks of gear teeth, International Organization for Standardization, 2013.
25. KissSoft. (2019). *KISSsoft release 2019 user manual*. Bubikon: KISSsoft AG - A Gleason Company.